Airborne and shipborne polarimetric measurements over open ocean and coastal waters: intercomparisons and implications for spaceborne observations

Matteo Ottaviani[a,d], Robert Foster[a,h], Alexander Gilerson[a*], Amir Ibrahim[b,c], Carlos Carrizo[a], Ahmed El-habashi[a], Brian Cairns[d], Jacek Chowdhary[d,e], Chris Hostetler[f], Johnathan Hair[f], Sharon Burton[f], Yongxiang Hu[f], Michael Twardowski[g], Nicole Stockley[g], Deric Gray[h], Wayne Slade[i], Ivona Cetinic[b,c]

[a]The City College of New York, CUNY, New York, NY 10031
[b]Universities Space Research Association, Columbia, MD 21044
[c]NASA Goddard Space Flight Center, Greenbelt, MD 10025
[d]NASA Goddard Institute for Space Studies, New York, NY 10025
[e]Columbia University, New York, NY 10025
[f]NASA Langley Research Center, Hampton, VA 23681
[g]Harbor Branch Oceanographic Institute, Fort Pierce, FL 34946
[h]Naval Research Laboratory, Washington, DC 20375
[i]Sequoia Scientific Inc., Bellevue, WA 98005

* Corresponding author: gilerson@ccny.cuny.edu

Abstract

Comprehensive polarimetric closure is demonstrated using observations from two in-situ polarimeters and Vector Radiative Transfer (VRT) modeling. During the Ship-Aircraft Bio-Optical Research (SABOR) campaign, the novel CCNY HyperSAS-POL polarimeter was mounted on the bow of the R/V Endeavor and acquired hyperspectral measurements from just above the surface of the ocean, while the NASA GISS Research Scanning Polarimeter was deployed onboard the NASA LaRC's King Air UC-12B aircraft. State-of-the-art, ancillary measurements were used to characterize the atmospheric and marine contributions in the

VRT model, including those of the High Spectral Resolution Lidar (HSRL), the AErosol RObotic NETwork for Ocean Color (AERONET-OC), a profiling WETLabs ac-9 spectrometer and the Multi-spectral Volume Scattering Meter (MVSM). An open-ocean and a coastal scene are analyzed, both affected by complex aerosol conditions. In each of the two cases, it is found that the model is able to accurately reproduce the Stokes components measured simultaneously by each polarimeter at different geometries and viewing altitudes. These results are mostly encouraging, considering the different deployment strategies of RSP and HyperSAS-POL, which imply very different sensitivities to the atmospheric and ocean contributions, and open new opportunities in above-water polarimetric measurements. Furthermore, the signal originating from each scene was propagated to the top of the atmosphere to explore the sensitivity of polarimetric spaceborne observations to changes in the water type. As expected, adding polarization as a measurement capability benefits the detection of such changes, reinforcing the merits of the full-Stokes treatment in modeling the impact of atmospheric and oceanic constituents on remote sensing observations.

Keywords: Vector Radiative Transfer, Polarization, Ocean Color, Aerosol Remote Sensing

1. Introduction

Within the discipline of ocean color, many attempts to obtain the optical and microphysical parameters of submarine particulates often reveal mismatches between data and simulations, deriving from the large variability of the water Inherent Optical Properties (IOPs), especially regarding the scattering properties of the samples (Brown and Gordon, 1973; Jonasz and Prandke, 1986; Loisel and Stramski, 2000; Loisel et al., 2008) and poorly understood spectral behaviors (Kostadinov et al., 2009). This complexity is exacerbated in coastal waters, where the input from freshwater sources usually cause the amount of Color Dissolved Organic Matter (CDOM) to spike, and the ocean color is affected by a multitude of additional substances such as minerals and detrital matter originating from rivers and run-offs. In addition, mechanical stressors like waves and tides contribute to turbulent mixing.

Early advances in polarimetric remote sensing (Hansen and Travis, 1974, Cairns et al.,

1999) have been demonstrated to provide unique constraints on the determination of the optical and microphysical properties of atmospheric particulates suspended both over ocean (Chowdhary et al., 2012; Ottaviani et al., 2012a) and land (Waquet et al., 2009), such as the parameters defining their size distributions and both real and imaginary parts of their complex refractive index, recognized as a proxy for the chemical composition. Obvious interest now exists in expanding this potential to the detection of characteristics of underwater particulates (Chami et al., 2001; Chami and Platel, 2007; Tonizzo et al., 2009; Lotsberg and Stamnes, 2010; Ibrahim et al., 2016). The fundamental issue concerning the application of polarimetry-based techniques to the retrieval of oceanic parameters from space is that the polarization signatures of light emerging from the water body are generally small in magnitude because 1) the relative index of refraction of the particulates is much smaller than for atmospheric particles (1.04-1.06 for organic and 1.15-1.20 for inorganic particles), 2) of multiple scattering effects and 3) the directions of scattered light with the maximum degree of polarization is usually outside the Snell's window and are not detectable above the water surface. These signatures also tend to be further washed out as the radiance from the water body travels through the air-water interface (Tonizzo et al., 2011; Mobley, 2015; Foster and Gilerson, 2016), and especially through the highly polarizing atmospheric medium where scattering generates up to 90% of the visible signal at the top of the atmosphere (TOA), in addition to the large impact of surface processes such as the glint caused by the specular reflection of the direct solar beams (Ottaviani et al., 2008a). Starting from the pioneering efforts to understand the submarine polarization light field in the 1950s (Waterman, 1954), progressively better matches between experimental data, theoretical analyses and numerical simulations were achieved in the following decades (Ivanoff et al., 1961; Timofeeva, 1961; Voss and Fry, 1984; Adams et al., 2012; Kattawar, 2013). Organic particles are weak scatterers because of their low refractive indices (Aas, 1996), and therefore modulate the underwater DoLP primarily via their absorption coefficient. In Case I waters, this leads to a small decrease in the DoLP compared to that of pure seawater, with observed maximum DoLPs of ~0.7 (Chami et al., 2001). These maxima occur at around 90° from the direction of propagation of the transmitted beam since, unlike reflection, transmission across the interface does not introduce significant polarization (<5% for Solar Zenith angles up to 80°, see e.g. Kattawar and Adams (1989)). Conversely, in Case II waters the higher refractive indices of inorganic particles (Babin et al., 2003) imply more complex scattering patterns (as is the case for atmospheric aerosols), which can be used in principle to distinguish them from organics (Chami, 2007; Lotsberg and Stamnes, 2010). However, the significant amounts of minerals typically found in coastal waters also favor multiple scattering, which suppresses the polarization originating from the single-scattering properties and yields maximum DoLPs of ~0.2-0.4 (Tonizzo et al., 2009).

With the exceptions of the POLarization and Directionality of the Earth's Reflectances (POLDER) series of instruments (Fougnie et al., 2007), decommissioned in 2013, and the Aerosol Polarimetry Sensor (APS) on board the Glory mission (Mishchenko et al., 2007) which however failed to reach orbit in 2011, no spaceborne polarimeter has yet been deployed. Therefore, several agencies worldwide presently advocate the use of dedicated polarimeters: JAXA's Second-generation GLobal Imager (SGLI) is scheduled for launch in 2017, while ESA/Eumetsat's Multi-Viewing Multi-Channel Multi-Polarization Imaging (3MI) and NASA's Plankton, Aerosol, Clouds, and ocean Ecosystem (PACE, (PACE Science Definition Team, 2012)) missions, specifically designed to assess the interplay between carbon cycle and climate, are projected to launch in 2021 and 2023, respectively. It is therefore imperative for the success of these forthcoming ocean color spaceborne platforms to explore the sensitivity of the polarized signal at the TOA to ocean and atmospheric constituents, in order to establish thresholds for detection. Recently, a few studies have targeted these space-based potential retrievals finding non-negligible polarization contributions at the shortest end of the spectrum over open ocean (Chowdhary et al., 2012; Harmel and Chami, 2008; Chami, 2007, Harmel, 2016) and at near-infrared wavelengths in coastal waters (Loisel et al., 2008), but also some signatures at wavelengths in the green (Ibrahim et al., 2016).

The focus of this paper is to demonstrate comprehensive closure between ship- and airborne measurements of polarized radiance and inherent optical properties for a variety of ocean and aerosol conditions using robust vector radiative transfer computations, which should be considered as a critical step toward the application of such measurements in advanced inversion models for atmospheric correction and the retrieval of additional water parameters. A description of the instrumentation is given in Sec. 2, followed by the description of the modeling approaches (Sec. 3) and the discussion on the match sought to the RSP and HyperSAS-POL observations (Sec. 4). To extend the application of the results to spaceborne observations, Sec. 5 presents the changes in total and polarized reflectance at the TOA caused by variations in the aerosol and oceanic parameters used to model the scenes. Such a study helps establishing the feasibility of space-based retrievals of the descriptive parameters.

2. Instruments and Method

2.1. SABOR field campaign

The NASA SABOR (Ship-Aircraft Bio-Optical Research) scientific mission took place from July 17 to August 7, 2014 in the Atlantic ocean off the US East Coast. The research vessel (R/V) Endeavor, operated by the Graduate School of Oceanography at the University of Rhode Island, sailed from Narragansett, RI into the Gulf of Maine. It then proceeded to Bermuda before returning to Narragansett through Norfolk, VA. The effort dealt with state-of-the-art measurements over a large range of water types, acquired through a redundant set of both remote-sensing and in situ instruments. Particular emphasis was placed on investigating the polarization signatures of ocean constituents, with the intention of improving the knowledge on critical biogeochemical processes and the links between photosynthetic activity and primary production.

The results are presented for a closure study that exploits in-situ measurements of water optical properties and atmospheric parameters collected from the R/V Endeavor, in order to simultaneously model through VRT simulations the spatially and temporally co-located observations from two spectropolarimeters: the HyperSAS-POL (City College of New York (CCNY)), installed on the mast of the ship, and the Research Scanning Polarimeter (RSP, NASA GISS) deployed together with the High-Spectral Resolution Lidar (HSRL) on the NASA Langley Research Center UC-12B aircraft, which overflew the ship at an altitude of ≈

9km. The observations analyzed in this work pertain to two very different water types: an open ocean station near Bermuda (LS6; July 27, 2014) and a near-coastal station in proximity of the CERES Ocean Validation Experiment (COVE) AERONET station (LS9; July 30, 2014). In Fig. 1, near real-time imagery from the MODerate-resolution Imaging Spectrometer (MODIS) on the Terra spacecraft is included for context. The LS6 station was characterized by exceptionally clear waters, while the location of the COVE platform is in more shallow, near-coastal waters at the mouth of the Chesapeake Bay, VA. In both cases, atypical aerosol loads with complex vertical stratification and spatial variability were present. Incidentally, the RSP had encountered a similar scenario with an outflow of absorbing aerosols over the COVE area in one of its early campaigns (Chowdhary et al., 2005). The difference in the remote sensing reflectance measured by the HyperSAS-POL sensor at the time of overpass at the two stations is plotted in the inset. In the following we provide a brief description of each instrument whose data was considered in our work, and explain the adopted methodology.

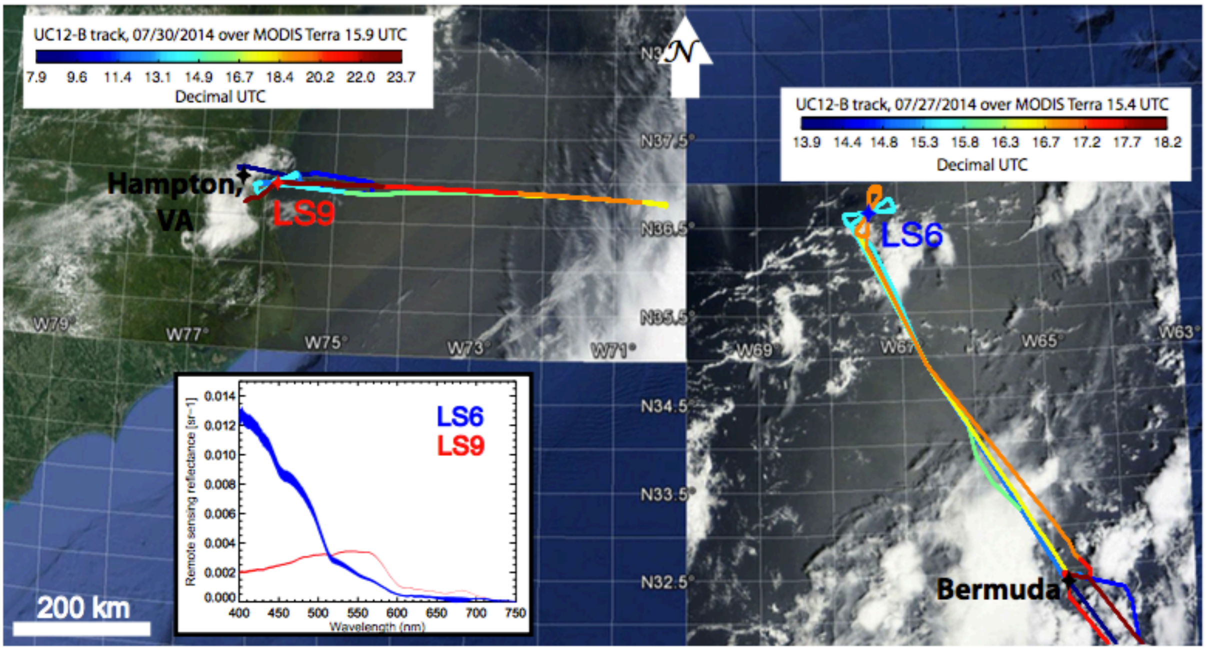

Figure 1: The color-coded segments illustrate the flight trajectory of the UC-12B involving overpasses at the location of the R/V Endeavor during the SABOR mission: station LS6 (open-ocean, 36.6512°N, 67.4267°W on 07/27/2014) and station LS9 (near-coastal, 36.9148°N, 75.8117°W on

07/30/2014). Near real-time imagery from the MODerate-resolution Imaging Spectrometer (MODIS), onboard the Terra platform, is overlaid to Google Earth. The inset in the lower left shows the remote sensing reflectance measured by the HyperSAS-POL instrument at the closest times to overpass. The shaded areas represent the standard deviation of 1-min averages close to the times of the UC-12B overpass at LS6 (blue) and LS9 (red).

2.2. Airborne instrumentation

Research Scanning Polarimeter. The Research Scanning Polarimeter (RSP) instrument is a multi-spectral photopolarimeter (Cairns et al., 1999) which for almost two decades has been deployed in a variety of field campaigns mainly aimed at aerosol research and atmospheric correction both over open ocean and coastal waters (Chowdhary et al., 2006, 2012; Ottaviani et al., 2012a) and different types of land surfaces (Waquet et al., 2009; Ottaviani et al., 2015). Its high accuracy and flawless performance promoted its design to serve as a prototype for the Aerosol Polarimeter Sensor (APS) planned to fly on the Glory space mission, which failed to reach orbit due to a rocket failure at launch. The RSP scans along track, and provides measurements of scene polarization at 152 viewing zenith angles symmetrically distributed around nadir (roughly ±50°), and at 9 wavelengths in the 410-2264 nm range. During SABOR, a few ”bowtie“ flight patterns were flown by the UC-12B aircraft over the R/V Endeavor during stations. It should be remarked that scanning along the principal plane (i.e., directly towards or away from the Sun) allows to collect the largest range of scattering angles. In our analysis, we indeed selected for station LS6 a transect closely aligned with the principal plane. Nevertheless, we report the results also for a scene where the relative azimuth was closer to the cross-principal plane direction, since it is instructive to examine the angular behavior of radiances and polarization in a region where the interfering effect of sunglint is minimized. In the case of station LS9, only one transect is analyzed with a relative azimuth of 33°, because of partial cloud interference during overpasses more closely aligned to the principal plane.

High Spectral Resolution Lidar. The High Spectral Resolution Lidar (HSRL, NASA Langley Research Center (Burton et al., 2015; Hair et al., 2008)) was mounted on the UC-

12B aircraft alongside the RSP. It provides vertical profiles of aerosol extinction at 532 nm and aerosol backscatter and depolarization at 532 and 1064 nm, independently from the Rayleigh contribution, i.e. without the need of assuming a lidar ratio. Regarding the optimal way to employ this information, the quantitative parameters directly usable as input to our radiative transfer simulations are the Aerosol Optical Thickness (AOT) at 532 nm and the aerosol vertical distribution, both accurately estimated (ΔAOT < 0.01 at 532 nm (Rogers et al., 2009)) at all altitudes in the curtain below the aircraft along the flight track. In addition, we used the dust mixing ratio product to define the amount of dust when preparing the aerosol mixture. Due to the monodirectionality of the laser pulse, other information can only be used qualitatively.

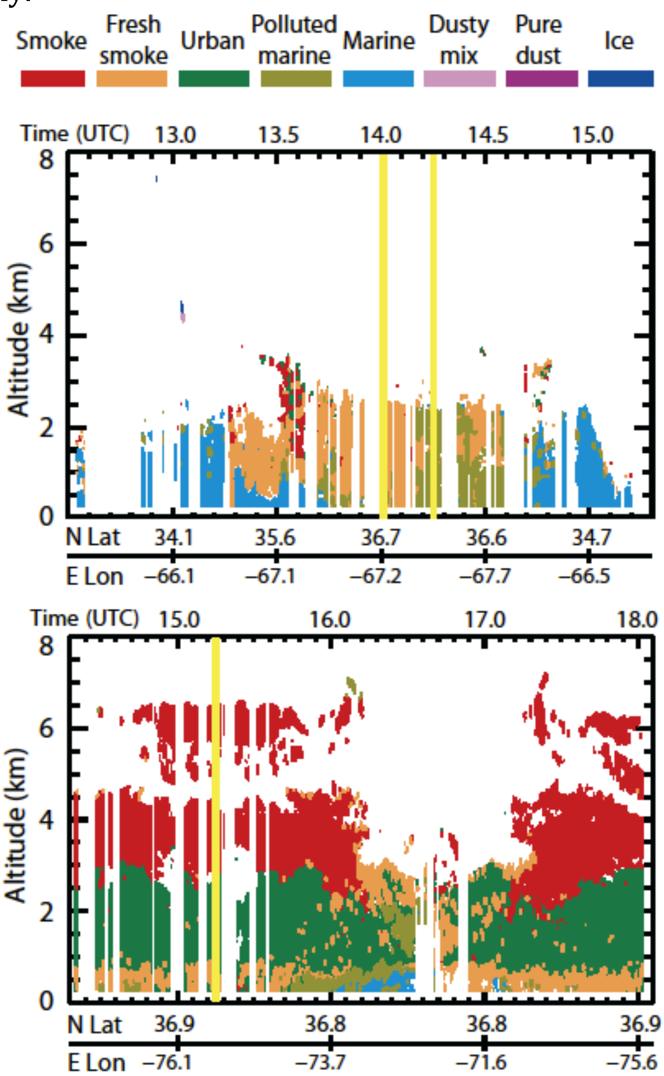

Figure 2: Results from the typing algorithm based on the HSRL measurements of aerosol

backscatter and extinction, for the UC12-B legs including the overpasses at stations LS6 (*upper panel*) and LS9 (*lower panel*). The yellow lines indicate the exact time of overpass. The presence in both scenes of variegate aerosol populations is evident.

For example, the lidar ratio (i.e., the inverse of the single scattering albedo multiplied by the value of the phase function at 180° (Young et al., 2013)) is sensitive to absorption but also to other parameters; since the phase function is not measured over the entire 180° range, the SSA cannot be calculated. Also, it is not possible to convert the backscattering Angström exponent into the extinction Angström exponent at a different wavelength without significant assumptions about the wavelength dependence of the lidar ratio. The post-processing of HSRL data has been recently augmented with an aerosol typing product based on cluster analysis of previous campaigns (Burton et al., 2012). The results of this algorithm along transects examined here are reported in Fig. 2, where yellow vertical lines mark the times of overpass. This classification is of obvious help in selecting appropriate aerosol models in our simulations (although for LS9 the microphysical properties determined from AERONET can be used directly). It is immediately noticeable from the figure how both stations exhibit a complex aerosol situation, where the marine background is injected with a flow of polluted species and a smoky component, with evident stratification. While the marine and dust types are identified with high confidence, smoke and urban are easy to separate from other types, but harder to separate from each other. For example, the isolated, lofted plume at around 13.5 UTC in the upper panel is likely all smoke rather than a mix of smoke and urban. Moreover, the distinction between "fresh" and "regular" smoke is based on the lidar ratio, and historically has been associated with smoke plumes from more local sources (Burton et al., 2012). Recent advancements in the HSRL technology have also enabled the measurement of the subsurface extinction coefficient (Hair et al., 2008), although this capability was not exploited in our analysis since higher-resolution, in situ measurements were available from the WET Labs suite.

2.3. Shipborne instrumentation

Inherent Optical Properties (IOPs). The IOPs were obtained from two in-water instrument packages. The first, operated by HBOI, included a WET Labs ac-9 spectrophotometer and an ECO-BB9. The ac-9 was used to measure the combined absorption and attenuation coefficients of particulate and dissolved material and that relative to the dissolved fraction only, so that the coefficients for the particulate fraction could be derived by difference (Twardowski et al. 1999). Absorption measurements were corrected for scattering errors using the "proportional correction" method (Zaneveld et al. 1994). The ECO-BB9 measured backscattering coefficients (Sullivan et al. 2013). Vertical profiles of all these IOPs were binned to 1 m.

The other sensor package operated by NRL included the Multi-Spectral Volume Scattering Meter (MVSM; custom) paired with a LISST-100X particle size analyzer by Sequoia Scientific. The MVSM measures the hydrosols' volume scattering functions (VSF), $\beta(\lambda, \theta)$, in the 0.5°-179° range of scattering angles with 0.25° resolution (at 532 nm during SABOR). The forward peak (limited to scattering angles smaller than 13°) of the VSF measured by the MVSM was replaced with the forward scattering information provided by the LISST-100X, following the technique of Slade and Boss (2006).

HyperSAS-POL. The HyperSAS-POL instrument was recently built in the Optical Remote Sensing Laboratory at CCNY. It collects hyperspectral radiometric measurements at 180 wavelengths in the 305-905 nm range at a single azimuthal angle, and at viewing zenith angles of 40° (water sensors) and 140° (sky sensors). In its preliminary version, which underwent intercomparison studies (Harmel et al., 2011, 2012) with a SeaPRISM sunphotometer installed at the Long Island Sound Coastal Observatory (LISCO), part of the AERONET and AERONET Ocean Color networks, two of the three identical downward looking sensors were equipped with polarization filters. One filter has its transmission axis oriented at 0° (parallel to the ground in the laboratory frame), and the other at 45° from this direction, so that the total and linearly polarized intensities can be computed as explained in Sec. 3.

Just before the SABOR cruise the system was outfitted for shipborne operations, the polarization capability was extended to the sky measurements and the mounting structure redesigned to exploit the foremast so as to guarantee the most unobstructed view (Fig. 3).

Based on the ship GPS location and instantaneous heading, an automated script enables azimuthal rotation via a stepper motor, so that the observations can be maintained at 90° (or 270°) azimuth relative to the Sun. If this configuration is impeded by the limits of rotation or the guy-wires supporting the mast, a 135° (or 225°) relative azimuth is instead chosen. A tilt sensor records pitch, roll and yaw at high temporal resolution, which in the post-processing stage allows correcting the measured Stokes vector for the instantaneous attitude of the vessel. The down-welling irradiance is recorded alongside for normalization purposes (e.g., to calculate the remote-sensing reflectance, see e.g. Fig. 1).

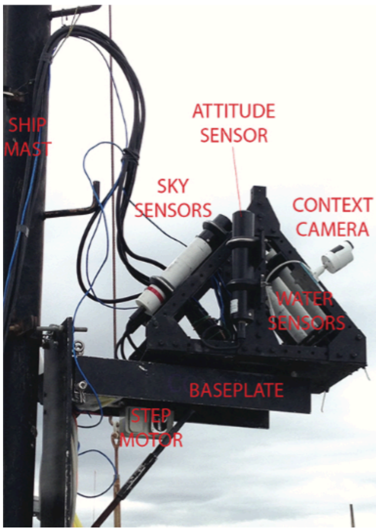

Figure 3: The HyperSAS-POL instrument mounted on the mast of the R/V Endeavor. An automated script fed by the ship navigational data commands a step-motor hidden below the baseplate to keep the instrument oriented towards sunglint-free angles.

Consistency of these radiometric hyperspectral polarization measurements above water, verified with VRT computations and comparisons with data from other instruments, is critical for further determination of the polarized water leaving radiance and remote sensing reflectance (Mobley, 2015, Foster and Gilerson, 2016). Characterization of such quantities, even in unpolarized mode, remains after several decades a topic of active discussion and research.

MICROTOPS II. Measurements of the AOT (at 380, 500, 675, 870 and 1020 nm) were carried out from the ship with a hand-held MICROTOPS II sunphotometer (Solar Light Company), operated by the CCNY group.

2.4. Other instrumentation

CIMEL SeaPRISM (AERONET-OC). For station LS9, AErosol RObotic NETwork (AERONET, (Holben et al., 1998)) measurements are available from the SeaPRISM instrument mounted on the COVE platform, in close proximity with the location of the R/V Endeavor. The SeaPRISM instrument consists of a CE-318 sunphotometer (CIMEL Electronique, France), and also makes radiometric measurements of the ocean water leaving radiance according to established protocols (AERONET-OC, (Zibordi et al., 2009)), with a downward looking angle of 40° from the nadir direction and at a relative azimuthal angle maintained at 90° to minimize the interference caused by sunglint. The spectral bands are centered around 413, 442, 491, 551, 668, 870 and 1018 nm. Given the abundance of in-water IOP measurements, only the atmospheric retrievals for this station were used in this work.

3. Radiative transfer computations

The RayXP package (version 2.04) is a 1-D, VRT code benchmarked against well-established Monte Carlo (Tynes et al., 2001) and VRT programs (Kokhanovski et al., 2010), and that excels for computational speed,thanks to efficient approaches to the solution of the radiative transfer equation (Zege et al., 1993; Zege and Chaikovskaya, 1996). The atmospheric and oceanic portions are fully coupled to include a flat or a wind-roughened surface, and the Stokes vector of the radiation field can be simulated at any point along the vertical coordinate of the Atmosphere-Ocean system in the near UV, Visible and IR spectral regions. To be of use as inputs to the code, the measurements of the water and atmospheric properties obtained from the instrumentation listed in the previous section must be converted into the total extinction, the single-scattering albedo, and the scattering matrices of aerosol and hydrosols. The ship anemometer provided the wind speed used to characterize the Cox-Munk distribution of wave slopes (Cox and Munk, 1954) that defines the surface roughness in the RayXP code.

Operationally, the Stokes vector parameters describing total intensity (I) and linearly polarized intensity (Q and U) are typically obtained from linear combinations of the radiances measured by sensors equipped with polarizing elements oriented at different angles (Hansen and Travis, 1974). For the RSP instrument, the linear combinations are

$$\begin{bmatrix} I \\ Q \\ U \end{bmatrix} = \begin{bmatrix} I_0 + I_{90} \\ I_0 - I_{90} \\ I_{45} - I_{135} \end{bmatrix} \quad (1)$$

where the subscripts indicate the orientations of the polarizers with respect to an arbitrary chosen frame of reference. Alternatively, as is the case for HyperSAS-POL, the Stokes parameters can be obtained from two sensors equipped with polarizers and one without (I_{TOTAL}):

$$\begin{bmatrix} I \\ Q \\ U \end{bmatrix} = \begin{bmatrix} I_{TOTAL} \\ 2I_0 - I_{TOTAL} \\ I_{TOTAL} - 2I_{45} \end{bmatrix} \quad (2)$$

If the same reference frame is chosen for Eqs. (1) and (2), the RSP and HyperSAS-POL measurements can be brought to closure by comparing them directly with the Stokes vector output by the model, run for the viewing geometry and altitude of the respective instrument.

3.1. Modeling of the oceanic portion

Regarding the oceanic portion, we take full advantage of the high vertical resolution (i.e., < 1 m) of the in situ measurements of IOPs. This resolution is less influential for the RSP than for the HyperSAS-POL, since the portion of atmosphere between the surface and the aircraft washes out much of the polarization details linked to the hydrosols' vertical distribution.

It has been observed (Morel 1973; Brown and Gordon, 1973; Jonasz and Prandke, 1986) that theoretical Mie calculations for hydrosols yield phase functions whose forward peak is underestimated compared to that obtained in the field. To mitigate this effect, the following steps were taken to incorporate the information available from the VSF measurements. First, measurements of the backscatter coefficient measured at the green and blue wavelengths made by the WET Labs ECO-BB9 sensors were averaged and extended to the red wavelengths (assuming the coefficients are spectrally flat). The particulate attenuation spectrum was then fitted to a power-law distribution, and the exponent from this fit was then used to estimate the particle size distribution (PSD) slope, assuming a Junge-type power law distribution (Boss et al. 2001). The slope is evaluated at each depth present in the IOP profile. For LS6, the near-surface slope is 4.04 and gradually increases to 4.38 at 80m depth. For LS9, the slope varied between 3.08 near the surface and 3.48 at the near-bottom depth of 9m. From the PSD slope and the measured backscattering ratio, the real part of the refractive index was inferred following the algorithm of Twardowski et al. (2001). The results are consistent with expectations; low refractive indices at LS6 (1.04-1.09) indicate largely biogenic molecules, while the more coastal LS9 exhibits slightly higher indices (1.12-1.15) representative of a bulk mixture of biogenic and mineral particles. The refractive index was used as an input to Mie calculations, which intrinsically assume a spherical shape for the hydrosols. A reduced scattering matrix was then computed by normalizing the Mie scattering matrix with respect to its (1,1) element. The MVSM measurements of the VSF, $\beta(\lambda,\theta)$, were normalized to the measured particulate scattering coefficient, $b_p(\lambda)$, to find the phase function:

$$\tilde{\beta}^{MVSM}(\lambda,\theta) = \frac{\beta(\lambda,\theta)}{b_p(\lambda)} = \frac{\beta(\lambda,\theta)}{2\pi\int_0^{\pi}\beta(\lambda,\theta)\sin\theta\, d\theta} \qquad (3)$$

In order to perform the integration in Eq. (3), the measured $\beta(\lambda,\theta)$ was extrapolated from 0.5° to 0° following a power-law relation, and the value measured at 170° was extended to 180°, since measurements at these backscattering angles are susceptible to unrealistic scattering peaks due to bubbles trapped in the instrument.

The "measured" phase matrix was finally obtained by multiplying all elements of the reduced matrix by the phase function in Eq. 3. In order to account for the benthic effects due to the shallow depth at LS9 (≈13 m), we modeled the albedo of the ocean floor (i.e., the bottom boundary condition in the radiative transfer simulations) as that typical of seagrass (Gilerson et al., 2013). For LS6, the water column is optically semi-infinite given the significant depth (≈ 5000 m), so the bottom can be safely modeled as a black surface.

3.2. Modeling of the atmospheric portion

To model the atmospheric portion, we employ a Rayleigh background and a mix of aerosols in layers whose physical thickness is taken from the HSRL observations. For both scenes, the HSRL reveals a complex aerosol situation characterized by different layers with very significant AOT (0.13 for LS6 and 0.34 for LS9, at 532 nm, see Tables 1 and 2). For the open-ocean station LS6, based on the results of the HSRL typing algorithm and the dust mixing ratio product (found in the column to vary between 8% and 10%), we exploited the aerosol models available in the RayXP library (Lenoble and Brogniez, 1984) and prepared a mixture where the background aerosol of the oceanic class was polluted with dust and soot (in a proportion by volume of 9% and 1%, respectively), homogeneously distributed below 3750 m. For LS9, aerosol properties are directly available from the AERONET measurements at COVE. Since the latter are intrinsically sensitive to the properties of an *effective* aerosol for the entire atmospheric column, only one layer was used with a top height of 6750 m, although the HSRL curtain shows the presence of two separated layers. The lofted smoke plume evident in its red color in Fig. 2, as physically thick as the lower layer, is anyway optically rather thin.

Based on various definitions for log-normal size distributions (Hansen and Travis, 1974; Dubovik et al., 2006; El-Hilo, 2012), the volume median radius and variance reported by AERONET were converted into the effective radius (r_{eff}) and effective variance (v_{eff}), accepted as input by the Mie code, by using the following equations:

$$r_{eff} = \frac{\int_{r_1}^{r_2} \frac{dV(r)}{d\ln r} d\ln r}{r_{eff}^2 \int_{r_1}^{r_2} \frac{1}{r} \frac{dV(r)}{d\ln r} d\ln r} \quad (4)$$

$$v_{eff} = \frac{\int_{r_1}^{r_2} \frac{(r - r_{eff})^2}{r} \frac{dV(r)}{d\ln r} d\ln r}{r_{eff}^2 \int_{r_1}^{r_2} \frac{1}{r} \frac{dV(r)}{d\ln r} d\ln r} \quad . \quad (5)$$

The numerical integration was performed after partitioning the log-normal volume particle size distribution dV(r)/dlnr (in units of $\mu m^3/\mu m^2$) into 22 logarithmically equidistant bins between 0.05 μm and 15 μm, a value that was found to be the optimal compromise between accuracy and computational time.

Table 1: Summary of descriptive parameters used to run the simulations for the observations at LS6 (July 27, 2014) and LS9 (July 30, 2014).

Parameter	Units	LS6	LS6	LS9
		(1st pass)	(2nd pass)	
Location	°	36.6521N, 67.4267W		36.9148N, 75.8117W
Water Depth	m	13		5000
UC-12B Overpass Time	UTC	14:01	14:15	15:15
AOT, 532 nm	unitless	0.13	0.13	0.34
Aerosol layer top height	m	3750	3750	6750
Windspeed	m/s	2.5	0.7	1.8

Solar Zenith Angle	°	38	36	31
Relative Azimuth	°	14	62	33

To obtain the spectral behavior of the AOT, we rescaled (to the value measured at 532 nm by the HSRL) the average of the MICROTOPS data obtained within 45 minutes from the overpass at LS6, and a temporally coincident AERONET Level 1.0 AOT spectrum for LS9. Unfortunately, the closest valid AERONET almucantar scan, which provides SSAs and refractive indices, took place one hour before the LS9 station overpass (see Table 1), when the Level 1.5 inversion data revealed an isolated case of decreased absorption, with the imaginary part of the refractive index plummeting from 0.0075 obtained from earlier and later spectra, to 0.0016.

It should also be noted that the AERONET inversions produce aerosol optical properties only at a few wavelengths in the 442-1016 nm range, limiting the knowledge on the properties of the coarse mode, which anyway has a contained effect on the shorter wavelengths of immediate interest for ocean color. The aerosol microphysical and optical properties were converted via mixing and Mie calculations to the scattering matrices needed to run the radiative transfer code. The resulting elements P11 (phase function) and P12/P11 (Degree of Linear Polarization) are illustrated in Fig. 4 for both stations, and for the wavelength of 550 nm.

Gaseous absorption is also accounted for by considering standard amounts of ozone, water vapor and nitrogen dioxide concentrations (each affecting selected RSP channels in different proportions). For LS9, direct measurements of precipitable water vapor were available from AERONET at COVE, averaged to a value of 2.7 cm.

Table 2: Summary of the closest AERONET products available for station LS9. The time of the UC-12B overpass was 15:15 UTC. The letters “f” and “c” specify quantities assigned to the “fine” and the “coarse” mode. The retrieval at 14:11:04 UTC was used to generate the third column in Fig. 6; the values were then manually adjusted in order to improve the fit for the visible and near-infrared channels (last column in this table and in Fig. 6).

Parameter	AERONET retrievals				Adj. model
	13:17:01	14:11:04	15:14:24	20:11:03	
AOT, 412nm	0.48	0.42	0.45	0.37	0.47
AOT, 532nm	0.35	0.30	0.33	0.26	0.33
AOT, 870nm	0.14	0.12	0.13	0.10	0.14
SSA, 442nm	0.961	0.990	N/A	0.979	0.964
SSA, 668nm	0.956	0.989	N/A	0.975	0.964
SSA, 870nm	0.947	0.986	N/A	0.970	0.943
Refr. Index, 442nm	1.50-0.007i	1.47-0.002i	N/A	1.55-0.004i	f: 1.47-0.007i c: 1.50-0.005i
Refr. Index, 668nm	1.49-0.007i	1.49-0.002i	N/A	1.52-0.004i	f: 1.50-0.005i c: 1.50-0.007i
Refr. Index, 870nm	1.50-0.007i	1.51-0.002i	N/A	1.52-0.004i	f: 1.47-0.007i c: 1.50-0.007i
Effective radius, μm	f:0.20 c:2.47	f:0.19 c:2.45	N/A	f:0.19 c:2.36	f:0.17 c:2.47
Effective variance	f:0.14 c:0.49	f:0.14 c:0.49	N/A	f:0.14 c:0.50	f:0.14 c:0.49
Fine mode fraction, %	98	98	N/A	98	98

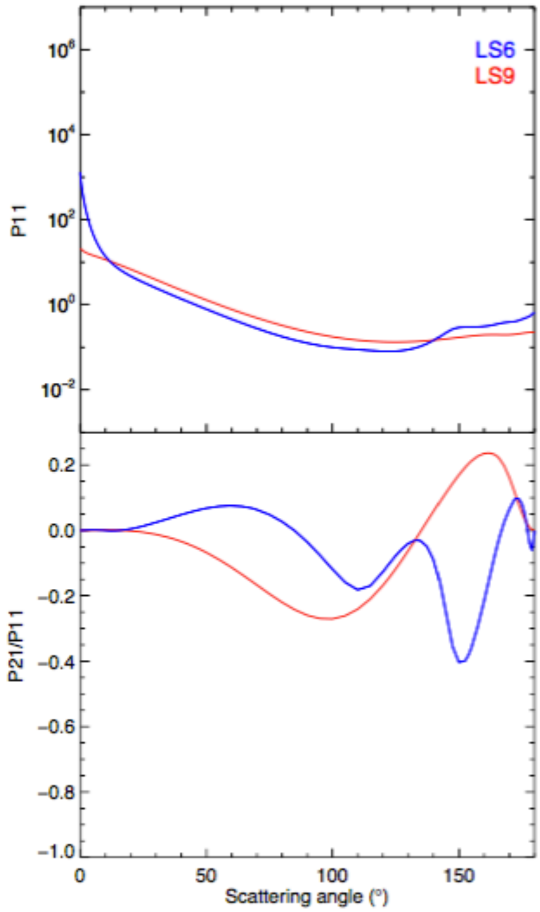

Figure 4: Scattering phase matrix elements P11 and P21/P11 at 550 nm, for the aerosol models obtained for the LS6 and LS9 stations. For LS6, note the strong forward scattering peak (nearly two orders of magnitude higher than for LS9), and the complex behavior of the degree of linear polarization for both stations in the backscattering hemisphere.

4. Results and Discussion

4.1. Water parameters

The left panels in Fig. 5 show the profiles of particulate scattering (b_p) and absorption (a_p) coefficients. The shallow water depth (≈13 m) at the LS9 station location explains the visibility of the continental shelf in the satellite imagery (Fig. 1, left panel). The right panel in Fig. 5 shows the volume scattering functions measured by the MVSM and the relative DoLP.

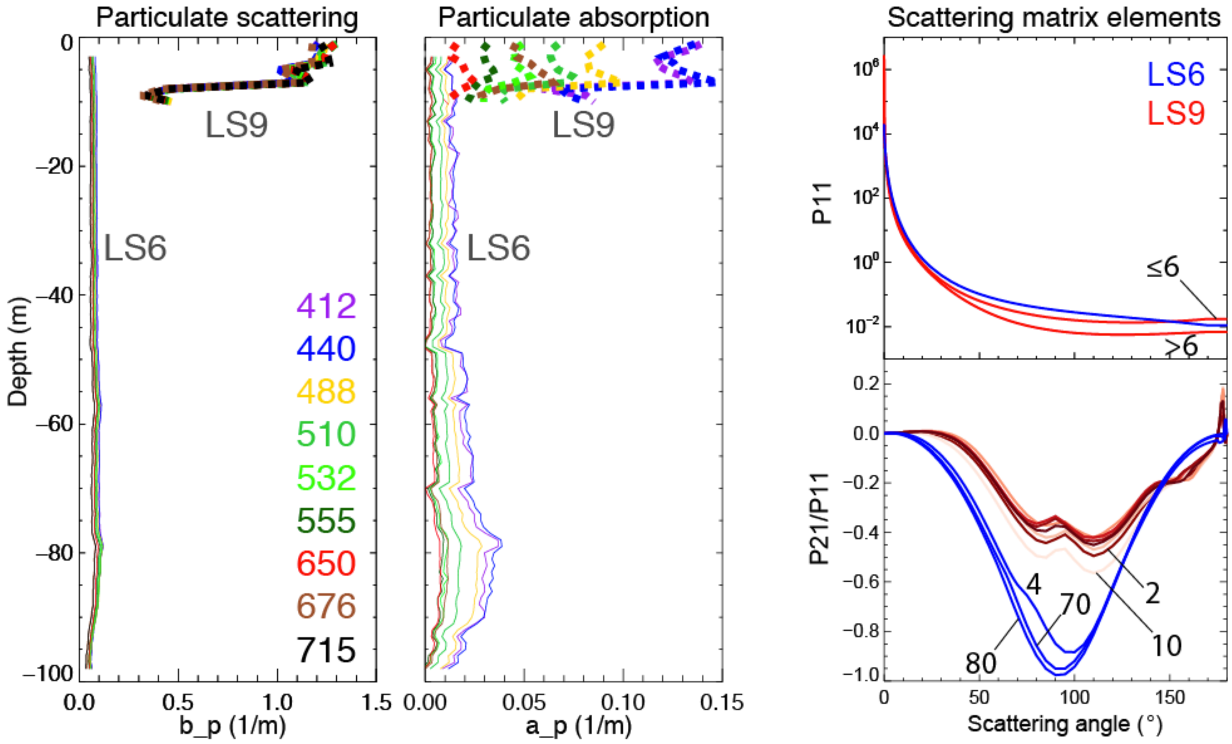

Figure 5: *Left panels*: vertical profiles of particulate scattering and absorption as measured by the ac-9 measurements for stations LS6 (solid lines) and LS9 (thick dotted lines) at the wavelengths indicated in color (the CDOM contribution is removed from the measured absorption). Note the marked increase in the scattering and absorption properties of the waters sampled at the near-coastal station LS9. *Right panel*: same as Fig. 4 (including the y-axes scales), but for the hydrosol models obtained for the LS6 and LS9 stations. The MVSM took measurements of P11 at a depth of 8 m. For LS9, one additional measurement was available at 3 m, which was used to describe the ocean layers above 6 m. For the DoLP, only 3 layers are shown for LS6 at depths as indicated by the numbers, in meters. For LS9, the polarization components resulting from the Mie simulations in 9 layers are indicated by fading shades of red, from the uppermost (2 m) to the deepest (10 m) layer.

While typically only one measurement was collected by the MVSM at a depth of 8 m, in the case of station LS9 one additional data point was available from a depth of 3 m. This value was used for layers above 6 m. The DoLP curves are instead a function of depth since they are derived from the Mie computations as described in Sec. 3.1. The details of the curves in this figure can be directly compared with those of Fig.4, and highlight the different scattering properties of aerosol and hydrosols. The angular behavior of the DoLP generated for station LS6 is very similar to that of Rayleigh scattering pertaining to pure water, peaking at a 90° scattering angle. Experimental observations with submerged polarimeters indeed show that the maximum DoLP in the underwater light field is found in this direction, although for waters rich in mineral particles the peak tends to shift toward 100° (Tonizzo et al., 2009), suggesting the possibility of using DoLP measurements to separate organic from inorganic species (Chami and Patel, 2007). Note also the pronounced backscattering peak of the optically complex water at LS9. As expected, the theoretical computations overestimate the peak magnitude (normally observed to be around 0.7 in open ocean and 0.4 in coastal waters), since multiple scattering, not accounted for in the Mie computations, suppresses polarization (Tonizzo et al. 2009).

4.2. Comparison of RSP measurements with VRT simulations

We first present the results related to the modeling of the RSP airborne measurements. The atmospheric and geometric input parameters used to initialize the VRT simulations are found in Table 1. Two RSP observations are used for the open-ocean LS6 station, the first corresponding to a transect overflying the ship at a direction oriented only 14° away from the solar principal plane (first column in Fig. 6, see the pronounced sunglint peak around a viewing zenith angle of 40°), and the second aligned instead closer to the cross-principal plane (Fig. 6, second column). In all panels, the solid lines represent the RSP measurements of the Stokes vector components in unit of radiance, as a function of downward-looking zenith angle, and color coded according to wavelength. The associated Degree of Linear Polarization (DoLP) is also reported. The dashed lines represent the results of the VRT simulations, and the y-axes have the common ranges indicated on the left.

The HSRL data (Fig. 2) shows that the "fresh smoke" dominating at the time of the first pass over station LS6 transitions to the "polluted marine" type just 15 minutes later, but these two types are often difficult to separate from each other since the distinction is based only on the backscatter color ratio. For consistency, the same aerosol model was used for both passes.

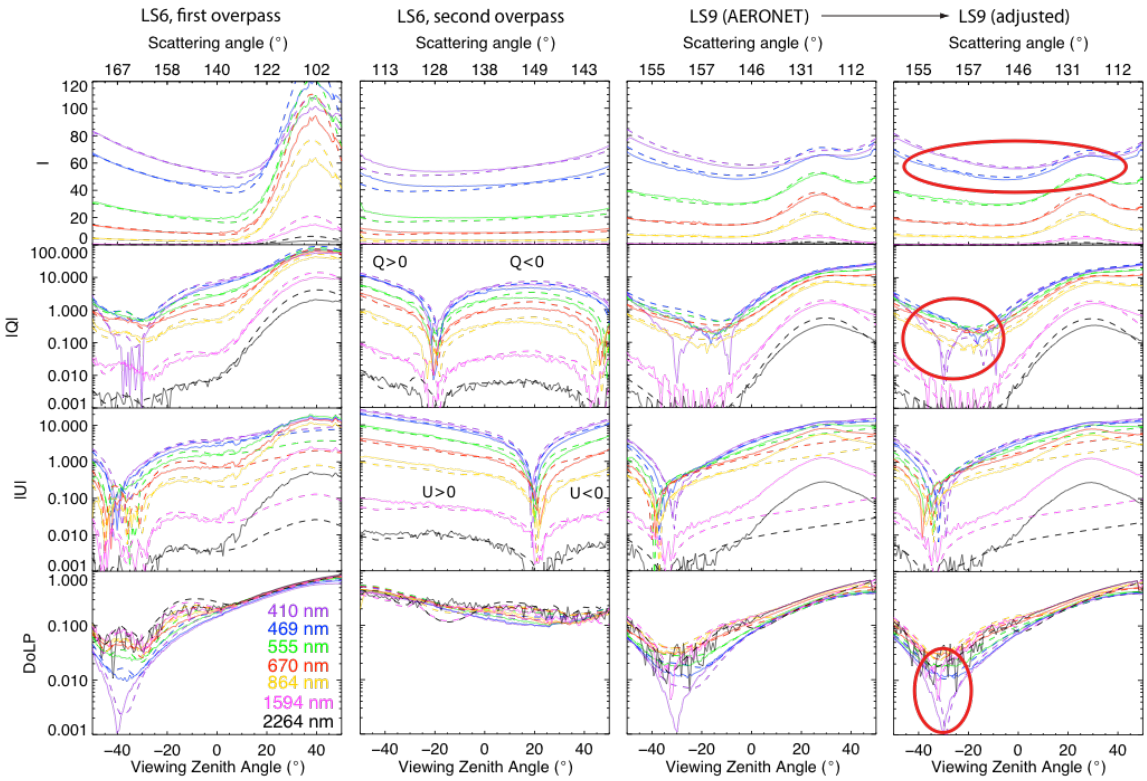

Figure 6: *First Column*: Research Scanning Polarimeter measurements (solid) and model (dashed), color coded at the indicated wavelengths, for a near principal plane pass (the relative azimuth was 14°) over station LS6. The Solar Zenith angle was 38°. The scattering angles corresponding to the RSP viewing zenith angles (bottom x-axis) and relative azimuth are indicated in the top x-axis. The units for I, Q and U are [W m^{-2} μm^{-1} sr^{-1}]. *Second column*: same as in the first column, but for a flight transect oriented at 62°. The Solar Zenith angle was 36°. In order to retain the information on the sign of the polarization components when plotting in logarithmic scale, positive and negative branches of Q and U are explicitly indicated. *Third Column*: Same as previous columns, but for station LS9 and a flight transect oriented at 33°. The Solar Zenith angle was 31°. *Fourth column*: same as the third column but with an adjusted aerosol model as reported in Table 2. Red ovals indicate areas of sensible improvements in the quality of the fit.

The fit to the RSP measurements for the near-principal-plane overpass at LS6 is of a very good quality, also considering that we used a mixture of prescribed aerosol models. The radiance associated with U exhibits much lower values than Q, as expected. The high polarization introduced by the mirror-like reflection causing the glint, rivaled only by Rayleigh scattering as a natural polarizer (Ottaviani et al., 2008b), is carried mostly by the Q component. The U component is identically zero when expressed relative to the scattering plane, yet in presence of multiple scattering and surface reflections a unique reference plane for the direct beam and all these other contributions can be defined only for observations taking place precisely in the solar principal plane. Here, Q and U are referred to the local meridional (scanning) plane (Ottaviani et al., 2012b). Within the glint region, the very similar mismatch between the measurements and the modeled values for Q and U (U is about 10 times smaller than Q, see y-axes) can be expected since the radiance and polarization exhibit large variability in response to a number of factors. For example, we neglect the wind direction (the Cox and Munk model is used in its first-order approximation). Also, the glint patch deviates from its ideal shape in the presence of local currents. Furthermore, small uncertainties in the knowledge of the aircraft attitude cause a small portion of the glint reflectance measured for the Q component to appear in the U component (Foster and Gilerson, 2016). Indeed, at 2264 nm, the surface signal travels virtually undisturbed through the atmosphere and is indeed non-negligible only in the glint region. This known behavior makes it an effective tool to retrieve the wind speed based on the Cox and Munk statistics (Cox and Munk, 1954), whenever in-situ anemometers are not available. In any case, a precise fit to the glint profile is less important here than evaluating the match at off-glint angles where the most of the scattering signatures are manifested. At these angles, the total radiance decreases as the wavelengths shifts towards the red and near-infrared region of the electromagnetic spectrum, an expected result due to the decreasing amount of Rayleigh and aerosol scattering. In the case of the second pass (Fig. 6, second column), some mismatch appears in the total radiance at the shortest wavelengths, very possibly originating from a decrease in the absorption properties of the fine mode in agreement with the HSRL observation. Once again, for consistency we kept the same aerosol model as during the first overpass when producing the results.

For the LS9 station, one off-principal plane observation is presented. The third column in Fig. 6 is obtained by using the results of the AERONET inversions at 14:11UTC (see Table 2) as an input to the simulations after rescaling the spectral AERONET AOT to the HSRL value at 532 nm at the time of overpass. It is evident how the AERONET inversion performs well when its products are used to model the total reflectance, but the fits to the polarization components Q and U are less than optimal. This result is explained considering that the descriptive parameters obtained from inversions based exclusively on measurements of total radiance cannot be expected to reproduce accurately the polarization state of the light field. In fact, polarization mismatches are observed in regions of lower radiance near backscatter (here at viewing zenith angles close to -40°), where the oscillations unique to each curve and the angular location of the points of polarization inversion (intercepts on the x-axis showing as cusps) greatly vary in response to small adjustments to the aerosol microphysical and optical properties. The rigorous search for an optimal fit can be achieved by non-linear inversions of the RSP data (see tailored algorithms in Ottaviani et al. 2012a, Knobelspiesse et al. 2011b), but even a small adjustment to the fine mode aerosol parameters (listed in Table 2) leads to an immediate improvement as shown in the rightmost column of Fig. 6. Note that the improvement occurs also for the total intensity at visible wavelengths, which is of interest to ocean color remote sensing.

4.3. Comparison of HyperSAS-POL measurements with VRT simulations

Figure 7 was obtained by taking the input files used to model the RSP data in Fig. 6, at the wavelengths significant to ocean color (410, 469, 555 and 670 nm), and changing the viewing geometry to mimic the HyperSAS-POL geometry. The left column pertains to station LS6 and the right column to station LS9. In both columns, the top panel is related to the upward-looking (“Sky”) sensors, and the middle panel to the downward-looking (“Water”) sensors. The Stokes vector elements I, Q, and U are depicted in blue, red and green color, respectively, as a function of the hyperspectral wavelengths. The thickness of the lines represents the standard deviation of the spectra within a 1-minute interval centered at the time of overpass. The four wavelengths available from the RSP are marked with open circles and connected by dashed lines, to visualize the overlap with the HyperSAS-POL spectra. The DoLP is in this case affected by noise because of the very small magnitude of I, Q and U especially at the longer wavelengths. A better quantity to be evaluated is the polarized radiance, $L^p = \sqrt{Q^2 + U^2}$, using error propagation from the primary Stokes components to estimate its uncertainty. Good matches are obtained for both the sky and water sensor, and at both stations. It is worth noting that for the water observations at LS9, the intensity is easily modulated by the specific model used for the bottom albedo. In the case of the seagrass model employed here, this effect is especially noticeable in the green, which can at least partially explain the slight mismatch at 555 nm. Degradations of the quality of the fit for Q and U below ≈480 nm is expected based on a progressive worsening of the diattenuation of the HyperSAS polarizers, and improvements to mitigate this effect are currently under evaluation (Foster, 2017). Occasional, less-than-perfect matches for the sky sensors' radiances are likely due to inhomogeneities in the aerosol distributions. Notwithstanding these exceptions, most of the simulated datapoints fall within the standard deviation of the measurements, which we consider to be a successful closure among the measurements.

The associated water-leaving radiances, Lw, isolated from the measurements by subtracting the diffuse sky contributions (estimated with simulations set to run with a black ocean body), are reported in the bottom row and exhibit typical differences between open and coastal waters. In Sec. 5 the discussion is expanded to consider the contributions of Lw to the radiances sensed at the TOA.

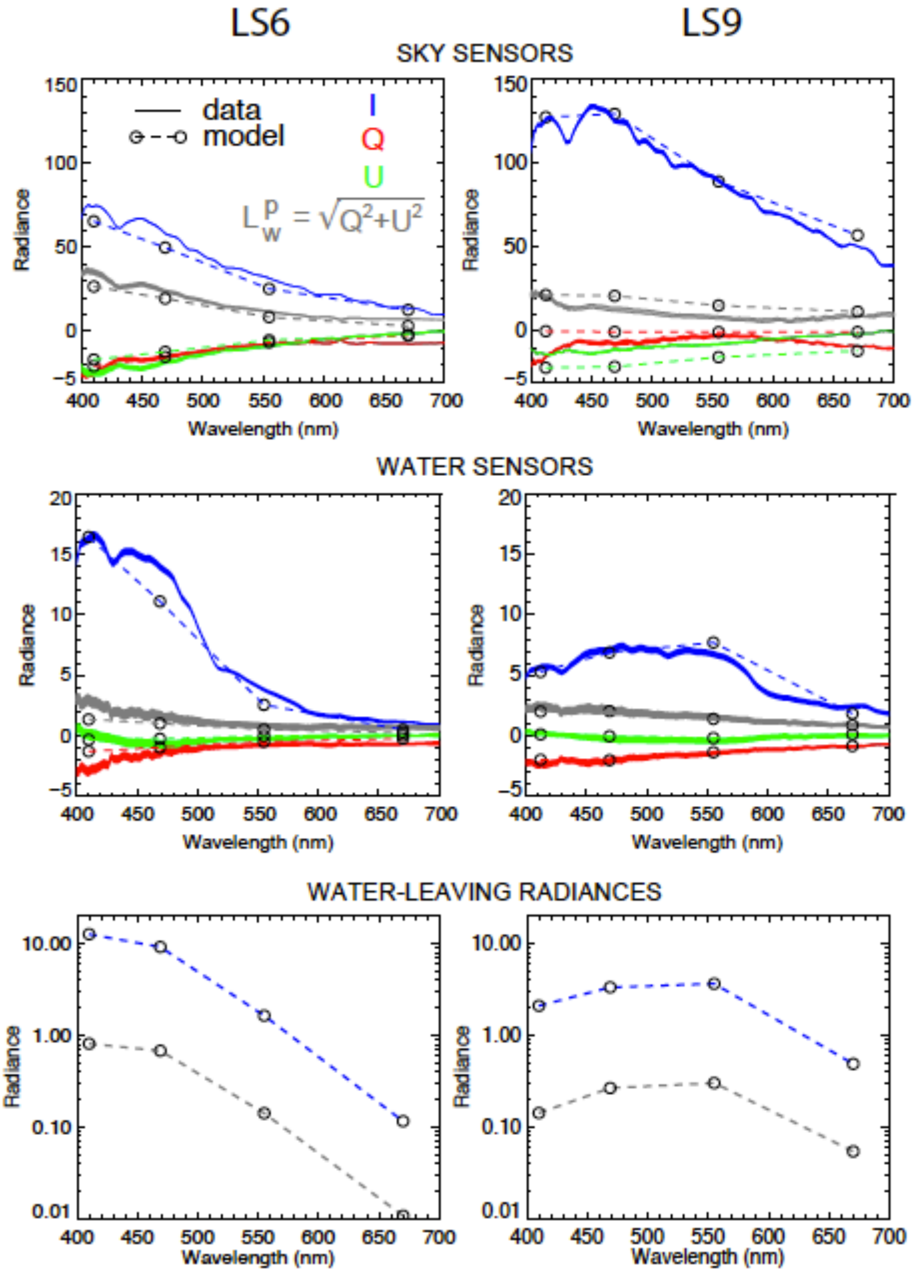

Figure 7: Comparison between the hyperspectral Stokes vector measured by the HyperSAS-POL instrument (*left*: LS6; *right*: LS9) and the derived polarized radiance, $L_w^p = \sqrt{Q^2 + U^2}$ (gray) with RayXP model results (open circles). The simulations were performed with the same atmospheric and oceanic inputs used to model the simultaneous RSP measurements (see Table 2 and Fig. 6), in order to demonstrate closure. The third row shows the total and polarized water-leaving radiances isolated from the measurements (note the log scale). The relative azimuth angles are 135° for LS6

and 225° for LS9. As in Fig. 6, the units of radiance are [W m^{-2} μm^{-1} sr^{-1}].

5. Sensitivity study for spaceborne observations

In this section we expand on our findings and simulate how a change in the descriptive parameters of the examined scenes would impact spaceborne observations, in line with similar studies (Chowdhary et al., 2006, 2012; Harmel and Chami, 2008). To this end, we use the same input files that successfully modeled the observations at stations LS6 and LS9, and calculate the Stokes components I, Q and U at the TOA for a complete grid of viewing angles (Fig. 9, 10). Here, the radial component represents the satellite downward viewing zenith angle and the azimuthal component is the azimuth relative to the Sun. The filled contours mimic the downward-looking total (R_I) and polarized (R_P) reflectances defined as:

$$R_I = \frac{\pi r_0^2}{F_0 \cos\theta_s} I \qquad (6)$$

$$R_P = \frac{\pi r_0^2}{F_0 \cos\theta_s} \sqrt{Q^2 + U^2} \qquad (7)$$

where F_0 is the exoatmospheric solar incident flux, r_0 is the Sun-Earth distance correction factor, and θ_s is the solar zenith angle. The reflectances R_Q and R_U are formed analogously. The use of these reflectances in place of I, Q and U has the advantage of nicely rescaling the Stokes vector by eliminating the dependence on the solar irradiance. Also, to analyze the polarization sensitivity in a remote sensing context, the polarized reflectance is a more appropriate quantity than the reflectances associated with the Stokes vector components themselves (Knobelspiesse et al., 2012). In fact, R_Q and R_U depend on the choice of a reference system while R_p does not, and the latter is more easily interpreted since it represents the fractional amount of polarized light entering a detector's field of view.

Removing particulate and CDOM extinction in shallow waters increases the contribution of the sea bottom albedo to the measured radiances. To remove this interference and safely compare with the open-ocean case, the deepest layer at LS9 was therefore extended to 5000 m so as to render LS9 as optically semi-infinite as LS6.

The results shown in Figs. 9 and 10 are organized in rows, each representing simulations at one wavelength. For the open ocean station, the selected wavelengths are in the visible while for the near-coastal stations we substituted the 470 nm with the 670 nm channel whose radiance in highly scattering waters can raise above the usual darkness displayed over open ocean (the results at all four wavelengths are anyway reported in Table 3, see below). The columns pertain to R_I, R_Q, R_U and R_P, respectively. The strong sunglint signal is immediately recognized along the principal plane, together with the decrease of scattering at longer wavelengths which suppresses the diffuse radiance.

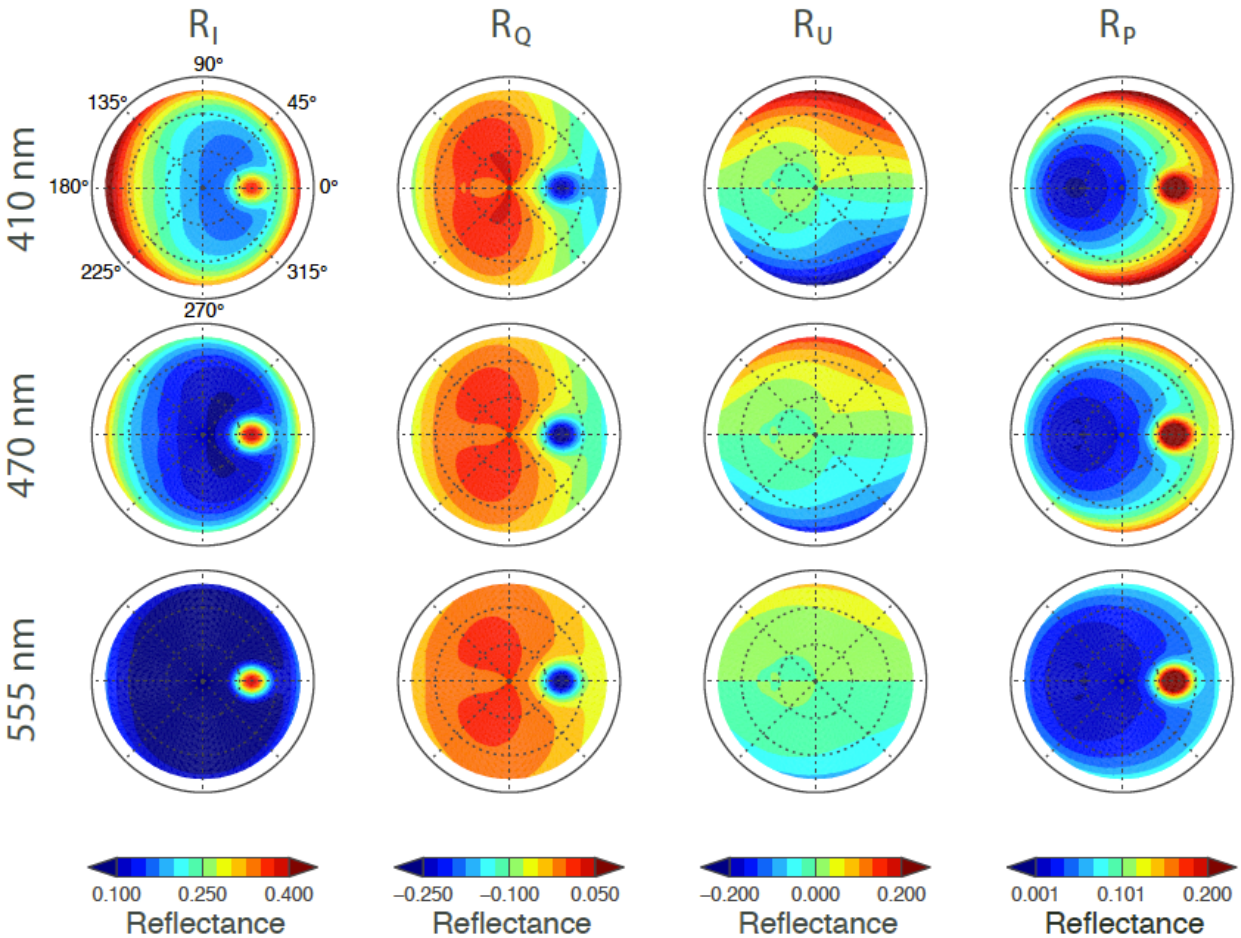

Figure 8: Reflectances associated with the Stokes parameters for the atmosphere-ocean system at the open-ocean station LS6, simulated at the top of the atmosphere for a downward-looking sensor at all viewing zenith (up to 80°) and azimuth angles.

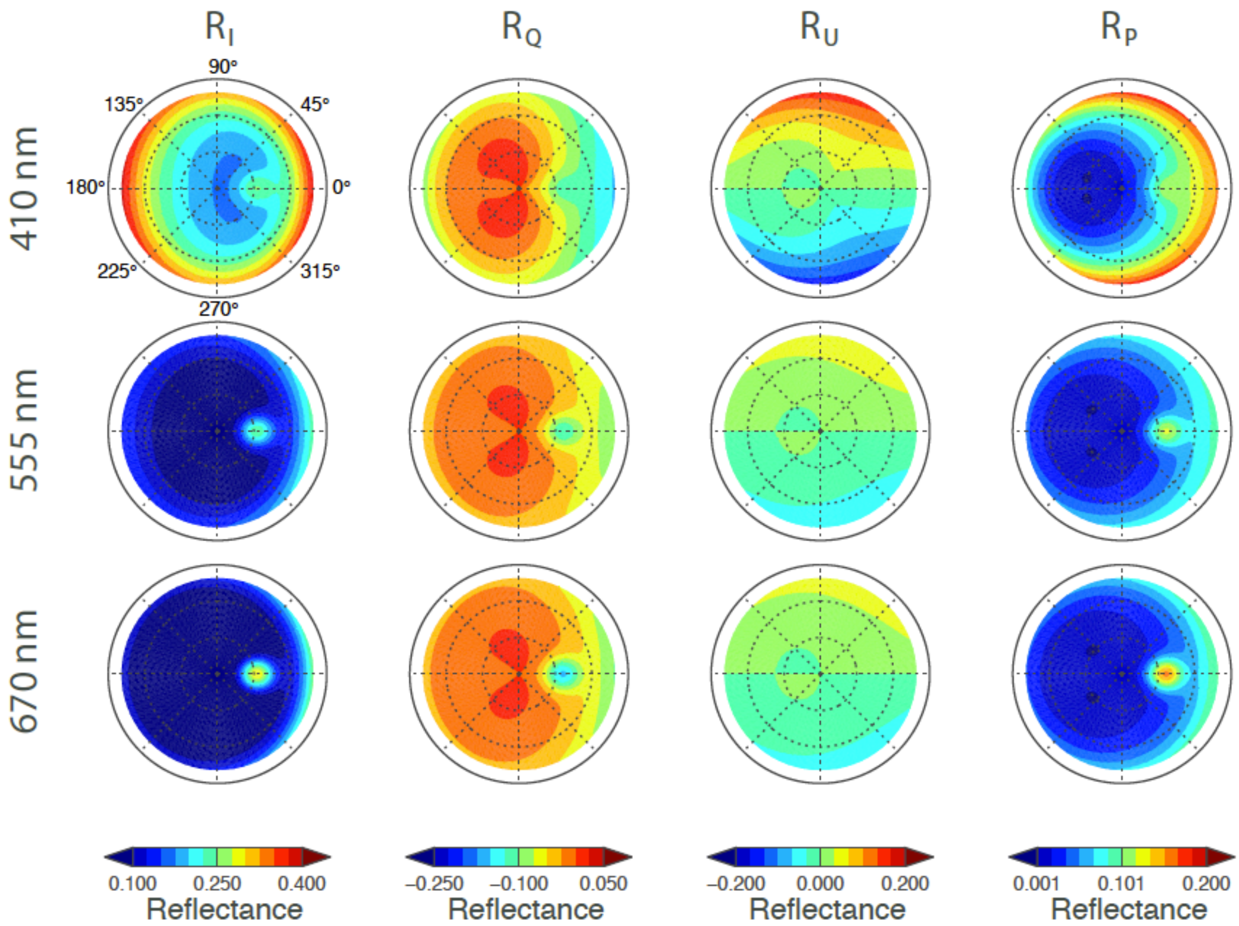

Figure 9: As in Fig. 8, including the colorbars' limits, but for the near-coastal station LS9 and with the 670 nm band substituting the one at 470 nm.

To follow up on Fig. 7, we examine the spectral contributions of the total and polarized water-leaving radiances to the radiances simulated at the TOA. The solid lines in the first row of Fig. 10 show the total (blue) and polarized (gray) water-leaving radiances. To isolate these contributions we subtracted, from the light field simulated just above the surface at each station, a second simulation where the ocean is set as a completely absorbing medium, i.e. an estimate of the diffuse skylight which is reflected from the surface (technically, this radiance still contains the sunglint contribution generated by the interface, which is however negligible at the HyperSAS-POL viewing geometry). The total water-leaving radiances at other viewing zenith angles along the HyperSAS-POL azimuthal planes of observation (135° for LS6, 225° for LS9) are similar and not shown, while the polarized water-leaving radiance can vary across one order of magnitude given the larger sensitivity of the scattering in the atmosphere-ocean system to the angle of observation. Such calculations can be contrasted with simulations run at the TOA (dashed lines) to evaluate the water-leaving spectral contributions to satellite observations. To this end, the panels in the bottom row report the ratio of the two signals, for both the total and the polarized radiance. As opposed to values reaching 15% for the total water-leaving radiance in the blue from clear waters, the largest contributions from coastal waters are found at wavelengths in the mid-visible. Note that these ratios agree very well with the results reported by Zhai et al. (2017) in a most recent work.

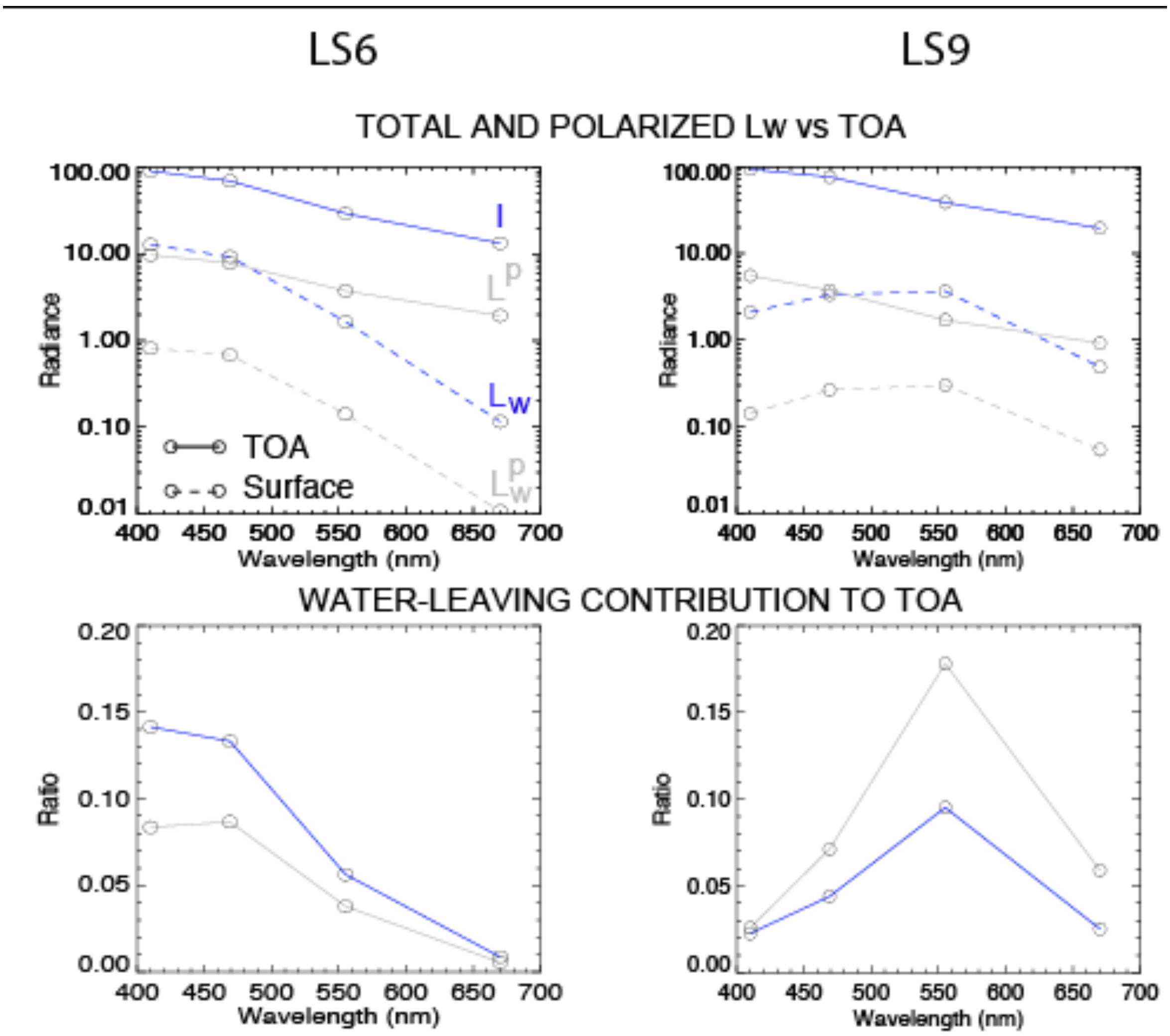

Fig. 10: Spectral water-leaving radiances (in [W m^{-2} µm^{-1} sr^{-1}]) at the two stations for a viewing zenith angle of 40° as in Fig. 7, but in relation to the radiances calculated for the same angle at the TOA (*top row*). The bottom row contains the ratio of such radiances to quantify the contribution of Lw to radiances remotely sensed from orbit.

For each station, we then consider the absolute differences in polarized reflectance, $|\Delta R_P|$, sensed at the TOA when the measured ocean IOPs are substituted for those of a pure-water ocean. Each maximum absolute difference in Table 3 is the maximum across all viewing geometries. To benefit from a more complete set of comparable scenarios, this value was also recalculated with (i) each station under an atmosphere where the sampled aerosols were substituted with a 2-km layer of the "oceanic" type from the RayXP library (with AOT_{532}=0.1, a scenario globally more typical of marine environments (Dubovik et al., 2002)) while maintaining the original spectral shape, and (ii) under a purely molecular atmosphere. The solar zenith angle at LS9 was set equal to that of LS6 (38°), and all simulations still contain the standard amount of gaseous absorption. Given the dark signals measured at LS9, for this station we also show how a plausible, three-fold increase in particulate scattering (again with AOT_{532}=0.1) affects only the wavelengths not dominated by CDOM absorption when the water is cleaned. To put all these results in context, the case is included where the aerosols were completely removed from the reference case, while the ocean IOPs were left unchanged with respect to those measured. In order to quantify the improvements provided by polarization observations, we consider a threshold corresponding to an absolute polarimetric calibration accuracy of 8.5×10^{-4}, in line with other studies (Chowdhary et al., 2012; Harmel and Chami, 2008). This threshold, derived as the noise equivalent signal for the POLDER sensor (along with the absolute radiometric accuracy of 4×10^{-4} (Fougnie et al., 2007)), is considerably higher than that achievable by RSP-like instruments, yet well suited to a conservative sensitivity study. Values of $\max(|\Delta R_P|)$ above the polarimetric threshold are in bold font.

It is found that the simulated changes are above the threshold for detection at the shortest wavelengths. With the total reflectance (not shown) exhibiting changes that justify the use of these bands for ocean color, the polarized reflectance at 410 nm and 470 nm adds further constraints in a hypothetical retrieval across viewing geometries accessible by satellite sensors. For the coastal station, the changes are close to the threshold also at the longer wavelengths. When considering the magnitude of these absolute differences two aspects are worth noting. Firstly, the threshold value chosen for R_p can be lowered of nearly an order of magnitude by current, demonstrated technologies (Cairns et al., 1999). Secondly, even if the polarized reflectance does not always exhibit detectable changes, during simultaneous retrievals it enhances the modeling of the atmospheric portion (i.e., the atmospheric correction), leading as a consequence to a more accurate retrieval of the ocean spectrum.

Table 3: Absolute maximum of the variation in polarized reflectance (Rp) simulated at the TOA when the ocean IOPs at LS6 and LS9 are substituted with those of a pure ocean, under the indicated conditions (with the exception of the last entry for each station, which considers removing the aerosols leaving the ocean IOPs as measured). The last entry in both cases illustrates the effect of removing only the aerosol load from the respective reference scene. Numbers in boldface are above the detection threshold established for POLDER ($\Delta Rp \geq 8.5 \times 10^{-4}$).

TOA Simulation, LS6	410 nm	470 nm	555 nm	670 nm
Reference Case (Fig. 11)	**8.7×10^{-3}**	**2.0×10^{-3}**	7.2×10^{-4}	1.4×10^{-4}
AOT_{532}=0.1§	**9.4×10^{-3}**	**2.1×10^{-3}**	7.7×10^{-4}	1.4×10^{-4}
No aerosols	**1.0×10^{-2}**	**2.2×10^{-3}**	8.4×10^{-4}	1.5×10^{-4}
Removing aerosols, water unchanged	**1.0×10^{-1}**	**1.3×10^{-1}**	**1.4×10^{-1}**	**1.6×10^{-1}**
TOA Simulation, LS9				
Reference Case (Fig. 12)	**9.4×10^{-3}**	**4.1×10^{-3}**	6.3×10^{-4}	2.3×10^{-4}
AOT_{532}=0.1§†	**1.5×10^{-2}**	**6.6×10^{-3}**	**9.6×10^{-4}**	3.3×10^{-4}
No aerosols†	**1.7×10^{-2}**	**7.1×10^{-3}**	**1.0×10^{-3}**	3.5×10^{-4}
$3 \times b_p$, AOT_{532}=0.1§†	**1.5×10^{-2}**	**5.6×10^{-3}**	**2.4×10^{-3}**	**9.3×10^{-4}**
Removing aerosols, water unchanged	**7.9×10^{-2}**	**9.5×10^{-2}**	**8.7×10^{-2}**	**8.0×10^{-2}**

§ The aerosol is of the "oceanic type" from the RayXP library.
† The Solar Zenith Angle was set to 38° as for LS6.

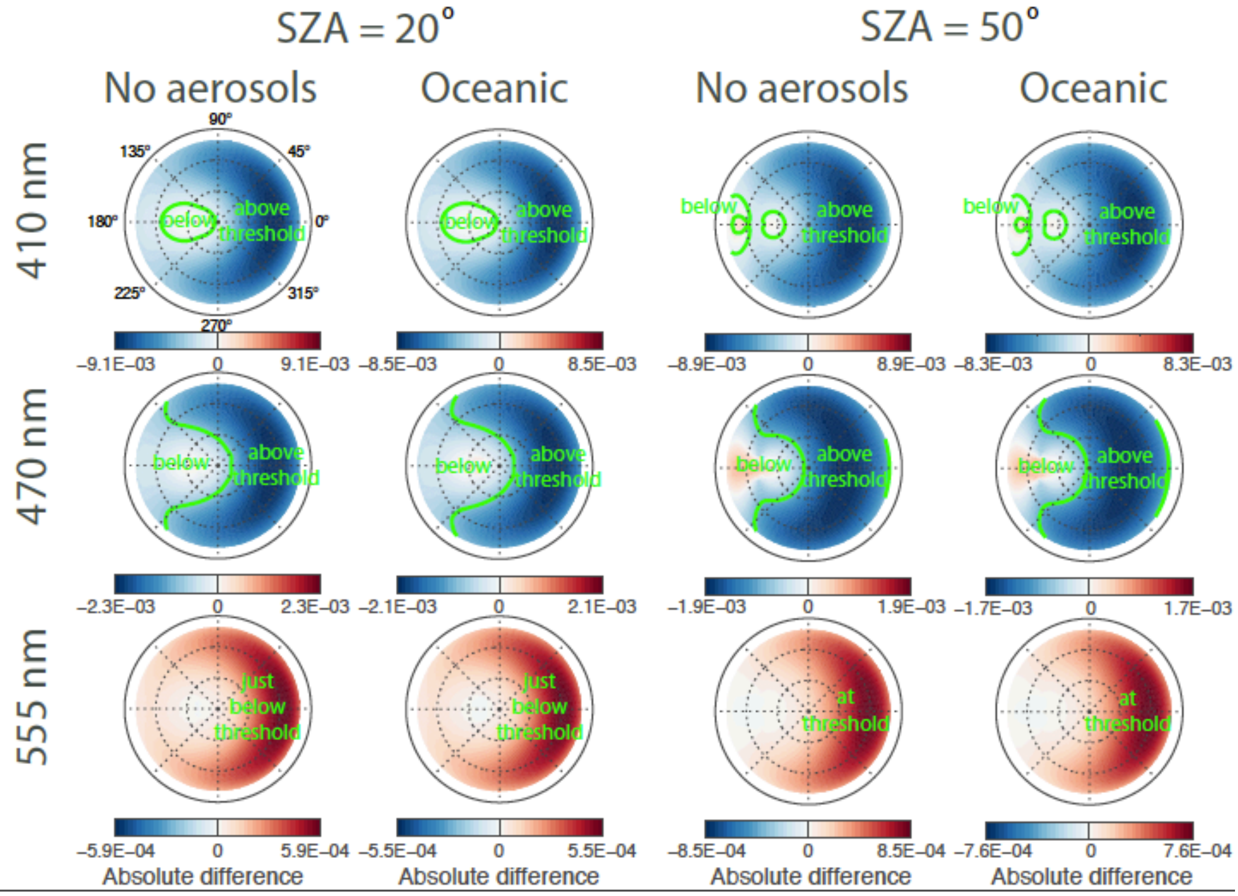

Figure 11: Absolute changes of TOA polarized reflectances at LS6 when a pure ocean is considered instead of the one characterized by the measured IOPs (Fig. 9), and under common atmospheric (no aerosol or with an oceanic type under 2km with spectrally flat AOT=0.1) and solar zenith angles (*left columns*: 20°; *right columns*: 50°). The angular ranges above and below the threshold for POLDER (see text) are highlighted.

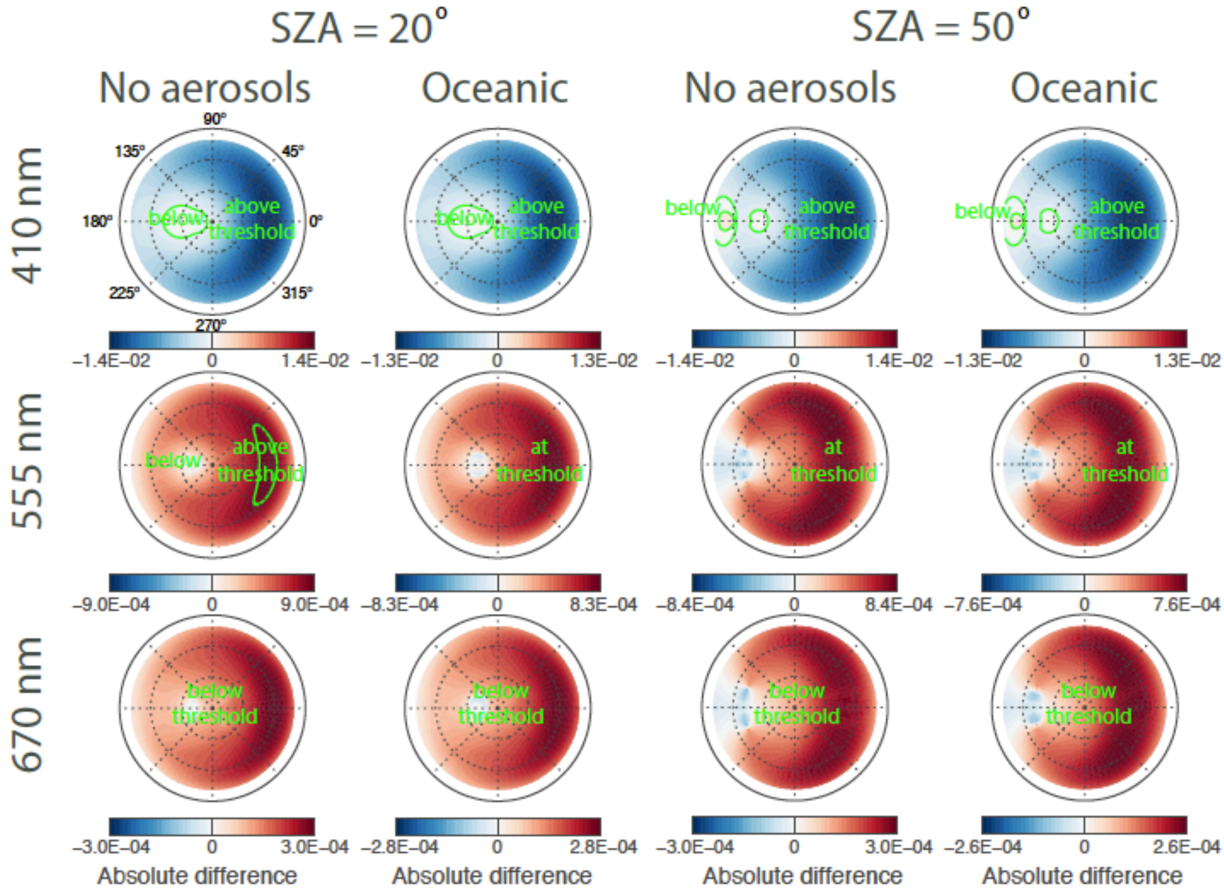

Figure 12: As in Fig. 11, but for the near-coastal station LS9 and with the 670 nm band substituting the one at 470 nm.

Regarding the impacts of variations in water type, removing the hydrosol component in the coastal environment obviously yields larger changes at the TOA than performing the same operation in the cleaner open-ocean scene. The combined effects of strong CDOM absorption and particulate scattering regulate the spectral details of this response, which remains well above the chosen conservative detection limit in the blue-green channels commonly exploited in ocean color retrievals. The changes are obviously masked by very heavy aerosol loads, which would hide the water from the satellite detector. Although not evaluated for a complete series of aerosol models, they are expected to depend weakly on aerosol type (which instead mostly affects the angular geometries at which said changes are detected). Removing the aerosols while leaving the ocean IOPs unchanged leads, as expected, to the absolute differences increasing of about one order of magnitude due to the established sensitivity of polarization to atmospheric particulates.

Figs. 11 (LS6) and 12 (LS9) give the angular details of the distribution of $\left|\Delta R_p\right|$ across all viewing geometries, for standardized atmospheric conditions and illumination geometries, so that the differences between the two water types obtained when removing the hydrosols can be directly compared. The maximum differences are found around regions where the scattering angle is around 90° (slightly closer to nadir for SZA=50° than for SZA=20°) and the polarization effects due to scattering are maximized, and which are typically accessible by satellite observations. At 410 nm and 555 nm, the differences at LS9 are larger than for the ``already blue'' waters at LS6. The comparison of the different columns in each figure does not reveal significant dependence of the magnitudes of Rp on solar zenith angle and on the presence aerosols in a moderate load (second and fourth column, AOT=0.1 at all wavelengths).

A few studies have focused on establishing the contribution of the polarized portion of the water-leaving radiance to the TOA (Zhai et al., 2017; Chowdhary et al., 2012; Harmel and Chami, 2008, Loisel et al., 2008). As pointed out in Chowdhary et al. (2012), some of these studies were limited to a single wavelength (470 nm in Harmel and Chami (2008) and 670 nm in Loisel et al. (2008)) or specific water types. To reconcile these conclusions, in Fig. 13 we show the straight absolute differences between the LS6 and LS9 waters, and for the same set of viewing geometries and atmospheric conditions as in Figs. 11 and 12 (at all the 4 wavelengths). The differences switch sign between 470 nm and 555 nm according to the relative magnitude of the polarized water leaving spectra. As in Figs. 11 and 12, no remarkable differences are noticed to occur as the SZA or the atmospheric particulate vary within typical values, although some interesting feature emerge near backscatter when the solar path is longer (SZA=50), revealing points of polarization inversion in the scattering phase functions. Once again, it is observed that the changes are mostly accessible at the shortest wavelengths. Nevertheless, they will become detectable also further toward the near infrared (and for a larger set of viewing geometries) as current technological advances improve POLDER-like performances, as shown by the contour lines of a second threshold corresponding to a higher, nowadays achievable accuracy (1×10^{-4}).

Even if sensitivity should not be taken as an absolute guarantee for parameter retrievability, the results indicate that, for typical AOTs, polarization measurements with accuracies presently achievable will boost the retrieval capabilities over both open ocean and coastal waters.

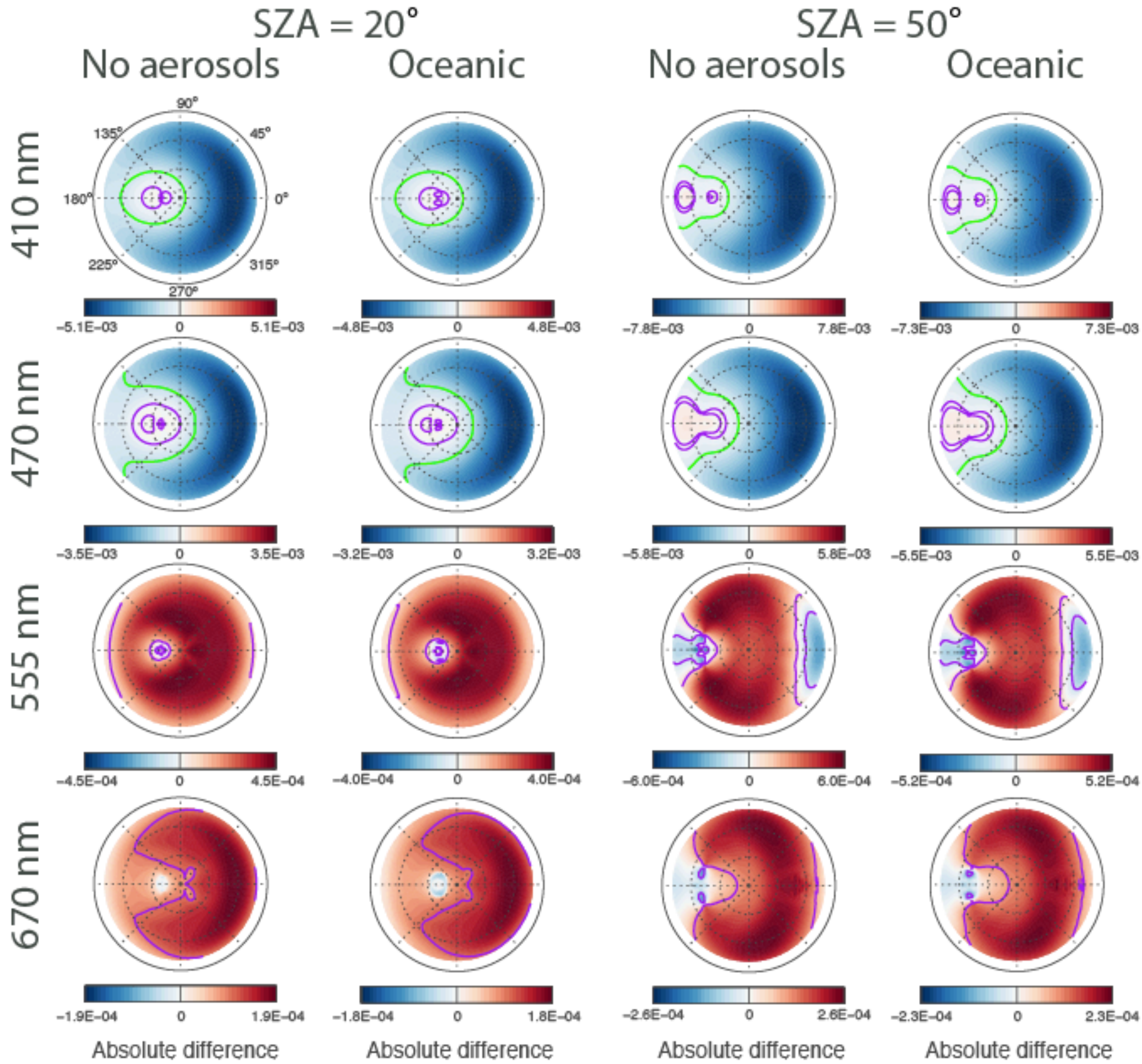

Figure 13: Absolute differences in polarized reflectance between the LS6 and LS9 water types, simulated at the TOA under the same atmospheric conditions and viewing geometries as in Figs. 11 and 12. The green contour lines correspond again to the POLDER threshold (8.5x10^{-4}); purple ones to an achievable higher accuracy (1x10^{-4}). The values at 555 nm and 670 nm are below the

POLDER threshold at all viewing geometries but become detectable at most viewing geometries with the new threshold.

6. Conclusions

Using the optical properties of aerosol and marine constituents determined from ancillary instruments, we successfully reproduced by means of rigorous vector radiative transfer computations the scene polarization measured simultaneously by two polarimeters (the shipborne HyperSAS-POL and the airborne RSP) for aircraft overpasses at the location of the R/V Endeavor during the SABOR cruise, in both clear open-ocean and coastal stations. In complex aerosol scenarios, the aerosol typing product from HSRL and the AERONET aerosol retrievals available for the coastal station helped to achieve a very good agreement with the measured components of the Stokes vector, although the AERONET retrievals were less accurate in reproducing the Q and U components, compatibly with the information content of measurements limited to total radiance. It also emphasizes the remarkable potential of combined polarimetric and lidar measurements, where the extraordinary sensitivity to particulate microphysical and optical properties is augmented by the lidar vertical resolution capabilities. The favorable comparison of HyperSAS-POL measurements to an established polarimeter such as the RSP also enables additional opportunities for shipborne above-water polarimetry. For example, the HyperSAS-POL technique can be extended to continuous measurements of sky and total water polarization during scientific cruises, and the water-leaving polarization signal effectively isolated and monitored as a function of water IOPs.

Our observations were also extrapolated to the TOA with the intent of estimating the impact of varying concentrations of oceanic constituents on satellite polarimetric observations. The results demonstrate the potential benefits of multi-angular polarization measurements in ocean color remote sensing with respect to observations based on total reflectance only. The simulated differences due to variations in the concentration of marine constituents are observable with the polarimetric accuracies achievable with state-of-the-art sensors, pending parallel improvements in the technology of in-situ packages devoted to the detailed characterization of marine IOPs.

8. Acknowledgments

We gratefully acknowledge support from the NASA Ocean Biology and Biogeochemistry Program and especially Program Manager Dr. Paula Bontempi who initiated and supported the SABOR cruise at all stages. We are also grateful to Dr. Michael Behrenfeld for his efforts in planning and coordinating the cruise. We owe a big thank you to the NASA AERONET staff and Dr. Brent Holben, site manager at COVE, for providing the aerosol properties used in part of the analysis. The satellite imagery used in Fig. 1 was downloaded from NASA Worldview. The RSP data are publicly available at http://data.giss.nasa.gov/pub/rsp. We are also very grateful to the two anonymous reviewers for their comment and suggestions, which significantly improved the quality of the manuscript. Finally, we are indebted for very constructive interactions with Drs. Knut Stamnes and Griet Neukermans.

9. References

Aas, E., 1996. Refractive index of phytoplankton derived from its metabolite composition. Journal of Plankton Research 18, 2223–2249.

Babin, M., Morel, A., Fournier-Sicre, V., Fell, F., Stramski, D., 2003. Light scattering properties of marine 520 particles in coastal and open ocean waters as related to the particle mass concentration. Limnology and oceanography 48, 843–859.

Boss, E., Twardowski, M.S. and Herring, S., 2001. Shape of the particulate beam attenuation spectrum and its inversion to obtain the shape of the particulate size distribution. Applied Optics, 40:4885-4893.

Brown, O.B., Gordon, H.R., 1973. Two component Mie scattering models of Sargasso Sea particles. Applied Optics 12, 2461–2465.

Burton, S.P., Ferrare, R.A., Hostetler, C.A., Hair, J.W., Rogers, R.R., Obland, M.D., Butler, C.F., Cook, A.L., Harper, D.B., Froyd, K.D., 2012. Aerosol classification of airborne high spectral resolution lidar measurements – 1. Methodology and examples. Atmospheric Measurement Techniques 5, 73–98.

Burton, S.P., Hair, J.W., Kahnert, M., Ferrare, R.A., Hostetler, C.A., Cook, A.L., Harper, D.B., Berkoff, T.A., Seaman, S.T., Collins, J.E., Fenn, M.A., Rogers, R.R., 2015. Observations of the spectral dependence of linear particle depolarization ratio of aerosols using NASA Langley airborne High Spectral Resolution Lidar. Atmospheric Chemistry and Physics 15, 13453–13473.

Cairns, B., Russell, E., Travis, L., 1999. Research Scanning Polarimeter: calibration and ground-based measurements. Proceedings of SPIE 3754, 186–196.

Chami M, Santer R, Dilligeard E., 2001. Radiative transfer model for the computation of radiance and polarization in an ocean-atmosphere system: polarization properties of suspended matter for remote sensing. Appl Opt.; 40 (15): 2398-416.

Chami, M., 2007. Importance of the polarization in the retrieval of oceanic constituents from the remote sensing reflectance. Journal of Geophysical Research: Oceans 112, C05026.

Chami, M., Platel, M.D., 2007. Sensitivity of the retrieval of the inherent optical properties of marine particles in coastal waters to the directional variations and the polarization of the reflectance. Journal of Geophysical Research: Oceans 112, C05037.

Chowdhary, J., Cairns, B., Mishchenko, M., Hobbs, P., Cota, G., Redemann, J., Rutledge, K., Holben, B., Russell, E., 2005. Retrieval of aerosol scattering and absorption properties from photopolarimetric observations over the ocean during the CLAMS experiment. Journal of the Atmospheric Sciences 62, 1093–1117.

Chowdhary, J., Cairns, B., Travis, L., 2006. Contribution of water-leaving radiances to multiangle, multispectral polarimetric observations over the open ocean: bio-optical model results for case 1 waters. Applied Optics 45, 5542–5567.

Chowdhary, J., Cairns, B., Waquet, F., Knobelspiesse, K., Ottaviani, M., Redemann, J., Travis, L., Mishchenko, M., 2012. Sensitivity of multiangle, multispectral polarimetric remote sensing over open oceans to water-leaving radiance: Analyses of RSP data acquired during the MILAGRO campaign. Remote Sensing of Environment 118, 284 –308.

Cox, C., Munk, W., 1954. Measurement of the Roughness of the Sea Surface from Photographs of the Sun's Glitter. Journal of the Optical Society of America 44, 838–850.

Dubovik, O., Holben, B., Eck, T., Smirnov, A., Kaufman, Y., King, M., Tanr´e, D., Slutsker, I., 2002. Variability of absorption and optical properties of key aerosol types observed in worldwide locations. Journal of the Atmospheric Sciences 59, 590–608.

Dubovik, O., Sinyuk, A., Lapyonok, T., Holben, B.N., Mishchenko, M., Yang, P., Eck, T.F., Volten, H., Munoz, O., Veihelmann, B., et al., 2006. Application of spheroid models to account for aerosol particle nonsphericity in remote sensing of desert dust. Journal of Geophysical Research: Atmospheres 111, D11208

El-Hilo, M., 2012. Nano-particle magnetism with a dispersion of particle sizes. Journal of Applied Physics 112, 103915.

Fougnie, B., Bracco, G., Lafrance, B., Ruffel, C., Hagolle, O., Tinel, C., et al., 2007. PARASOL in-flight calibration and performance. Applied Optics 46, 5435–5451.

Foster, R., Gilerson, A., 2016. Polarized transfer functions of the ocean surface for above-surface determination of the vector submarine light field. Applied Optics 55, 9476-9494.

Foster, R. The polarization of light in coastal and open oceans : ref lection and transmission by the air- sea interface and application for the retrieval of water optical properties, PhD Thesis, CCNY, 2017.

Gilerson, A.A., Stepinski, J., Ibrahim, A.I., You, Y., Sullivan, J.M., Twardowski, M.S., Dierssen, H.M., Russell, B., Cummings, M.E., Brady, P., et al., 2013. Benthic effects on the polarization of light in shallow waters. Applied optics 52, 8685–8705.

Hair, J., Hostetler, C., Cook, A., Harper, D., Ferrare, R., Mack, T., Welch, W., Isquierdo, L., Hovis, F., 2008. Airborne High Spectral Resolution Lidar for profiling aerosol optical properties. Applied Optics 47, 6734–6752.

Hansen, J., Travis, L., 1974. Light scattering in planetary atmospheres. Space Science Reviews 16, 527–610.

Harmel, T., 2016. Recent developments in the use of light polarization for marine environment monitoring from space," in Light Scattering Reviews, Springer, Vol. 10, 41–84.

Harmel, T., Chami, M., 2008. Invariance of polarized reflectance measured at the top of atmosphere by parasol satellite instrument in the visible range with marine constituents in open ocean waters. Optics Express 16, 6064–6080.

Harmel, T., Gilerson, A., Hlaing, S., Tonizzo, A., Legbandt, T., Weidemann, A., Arnone, R., Ahmed, S., 2011. Long Island Sound Coastal Observatory: assessment of above-water radiometric measurement uncertainties using collocated multi and hyperspectral systems. Applied optics 50, 5842–5860.

Harmel, T., Gilerson, A., Tonizzo, A., Chowdhary, J., Weidemann, A., Arnone, R., Ahmed, S., 2012. Polarization impacts on the water-leaving radiance retrieval from above-water radiometric measurements. Applied optics 51, 8324–8340.

Holben, B., Eck, T., Slutsker, I., Tanre, D., Buis, J., Setzer, A., Vermote, E., Reagan, J., Kaufman, Y., 585 Nakajima, T., et al., 1998. AERONET–A federated instrument network and data archive for aerosol characterization. Remote Sensing of Environment 66, 1–16.

Ibrahim, A., Gilerson, A., Chowdhary, J., Ahmed, S., 2016. Retrieval of macro-and micro-physical properties of oceanic hydrosols from polarimetric observations. Remote Sensing of Environment 186, 548–566.

Ivanoff, A., Jerlov, N., Waterman, T.H., 1961. A comparative study of irradiance, beam transmittance and 590 scattering in the sea near Bermuda. Limnology and Oceanography 6, 129–148.

Jonasz, M., Prandke, H., 1986. Comparison of measured and computed light scattering in the Baltic. Tellus B 38, 144–157.

Kattawar, G., Adams, C., 1989. Stokes vector calculations of the subma&e light field in an atmosphere-ocean with scattering according to a Rayleigh phase matrix: Effect of interface refractive index on radiance and polarization. Limnol., Oceanogr., 34 (8), 1453-1472.

Knobelspiesse, K., Cairns, B., Mishchenko, M., Chowdhary, J., Tsigaridis, K., van Diedenhoven, B., Martin, W., Ottaviani, M., Alexandrov, M., 2012. Analysis of fine-mode aerosol retrieval capabilities by different passive remote sensing instrument designs. Opt. Express 20, 21457–21484.

Knobelspiesse, K., Cairns, B., Redemann, J., Bergstrom, R., Stohl, A., 2011. Simultaneous retrieval of aerosol and cloud properties during the MILAGRO field campaign. Atmospheric Chemistry and Physics 600 11, 6245–6263.

Kokhanovsky, A.A., Budak, V.P., Cornet, C., Duan, M., Emde, C., Katsev, I.L., Klyukov, D.A., Korkin, S.V., C-Labonnote, L., Mayer, B., et al., 2010. Benchmark results in vector atmospheric radiative transfer. Journal of Quantitative Spectroscopy and Radiative Transfer 111, 1931–1946.

Kostadinov, T., Siegel, D., Maritorena, S., 2009. Retrieval of the particle size distribution from satellite 605 ocean color observations. Journal of Geophysical Research: Oceans 114.

Lenoble, J., Brogniez, C., 1984. A comparative review of radiation aerosol models. Beitraege zur Physik der Atmosphaere (ISSN 0005-8173), vol. 57, Feb. 1984, p. 1-20. 57, 1–20.

Loisel, H., Duforet, L., Dessailly, D., Chami, M., Dubuisson, P., 2008. Investigation of the variations in the water leaving polarized reflectance from the POLDER satellite data over two biogeochemical contrasted oceanic areas. Opt. Express 16, 12905–12918.

Loisel, H., Stramski, D., 2000. Estimation of the inherent optical properties of natural waters from the irradiance attenuation coefficient and reflectance in the presence of Raman scattering. Applied optics 39, 3001–3011.

Lotsberg, J., Stamnes, J., 2010. Impact of particulate oceanic composition on the radiance and polarization of underwater and backscattered light. Optics Express 18, 10432–10445.

Mishchenko, M., Cairns, B., Kopp, G., Schueler, C., Fafaul, B., Hansen, J., Hooker, J., Itchkawich, T., Maring, H., Travis, L., 2007. Accurate monitoring of terrestrial aerosols and total solar irradiance. Bulletin of the American Meteorological Society 88, 677–691.

Mobley, C., 2015. Polarized reflectance and transmittance properties of windblown sea surfaces, Applied Optics, 54, 4828-4849.

Morel, A., 1973. Diffusion de la lumiere par les eaux de mer. Rèsultats expèrimentaux et approche thèorique. Optics of the Sea 61, 3–1.

Morel, A., Maritorena, S., 2001. Bio-optical properties of oceanic waters-a reappraisal. Journal of Geophysical research 106, 7163–7180.

Ottaviani, M., Cairns, B., Chowdhary, J., Diedenhoven, B.V., Knobelspiesse, K., Hostetler, C., Ferrare, R., Burton, S., Hair, J., Obland, M.D., Rogers, R., 2012a. Polarimetric retrievals of surface and cirrus clouds properties in the region affected by the Deepwater Horizon oil spill. Remote Sensing of Environment 121, 625 389 – 403.

Ottaviani, M., Cairns, B., Ferrare, R., Rogers, R., 2012b. Iterative atmospheric correction scheme and the polarization color of alpine snow. Journal of Quantitative Spectroscopy and Radiative Transfer 113, 789 – 804.

Ottaviani, M., van Diedenhoven, B., Cairns, B., 2015. Photopolarimetric retrievals of snow properties. The Cryosphere 9, 1933–1942.

Ottaviani, M., Spurr, R., Stamnes, K., Li, W., Su, W., Wiscombe, W., 2008a. Improving the description of sunglint for accurate prediction of remotely sensed radiances. Journal of Quantitative Spectroscopy and Radiative Transfer 109, 2364–2375.

Ottaviani, M., Stamnes, K., Koskulics, J., Eide, H., Long, S., Su, W., Wiscombe, W., 2008b. Light reflection from water waves: Suitable setup for a polarimetric investigation under controlled laboratory conditions. Journal of Atmospheric and Oceanic Technology 25, 715–728.

PACE Science Definition Team, 2012. Pre-Aerosol, Clouds, and ocean Ecosystem (PACE) Mission Science Definition Team Report. Available at: http://decadal.gsfc.nasa.gov/.

Rogers, R., Hair, J., Hostetler, C., Ferrare, R., Obland, M., Cook, A., Harper, D., Burton, S., Shinozuka, Y., McNaughton, C., et al., 2009. NASA LaRC airborne high spectral resolution lidar aerosol measurements during MILAGRO: observations and validation. Atmospheric Chemistry and Physics Discussions 9, 8817– 8856.

Sullivan, J., Twardowski, M., Zaneveld, J.R.V. and C. Moore, 2013. Measuring optical backscattering in water, In: A. Kokhanovsky (Ed), Light Scattering Reviews 7: Radiative Transfer and Optical Properties of Atmosphere and Underlying Surface, Springer Praxis Books, doi: 10.1007/978-3-642-21907-8_6, 189-224.

Slade, W.H., Boss, E.S., 2006. Calibrated near-forward volume scattering function obtained from the lisst particle sizer. Optics Express 14, 3602–3615.

Stockley, N., Röttgers, R., McKee, D., Sullivan, J., M., T., 2016. Absorption measurements from an in-water reflective tube absorption meter: assessing uncertainties for different scattering correction algorithms. Optics Express, submitted.

Timofeeva, V., 1961. On the problem of polarization of light in turbid media. Izvestiya Geophysics 5, 766–774.

Tonizzo, A., Gilerson, A., Harmel, T., Ibrahim, A., Chowdhary, J., Gross, B., Moshary, F., Ahmed, S., 2011. Estimating particle composition and size distribution from polarized water-leaving radiance. Applied Optics 50, 5047–5058.

Tonizzo, A., Zhou, J., Gilerson, A., Twardowski, M.S., Gray, D.J., Arnone, R.A., Gross, B.M., Moshary, F., Ahmed, S.A., 2009. Polarized light in coastal waters: hyperspectral and multiangular analysis. Optics Express 17, 5666–5683.

Twardowski, M.S., Sullivan, J.M., P.L. Donaghay, P.L. and Zaneveld, J.R.V., 1999. Microscale quantification of the absorption by dissolved and particulate material in coastal waters with an ac-9. Journal of Atmospheric and Oceanic Technology, 16(12):691-707.

Twardowski, M., Zhang, X., Vagle, S., Sullivan, J., Freeman, S., Czerski, H., You, Y., Bi, L., Kattawar, G., 2012. The optical volume scattering function in a surf zone inverted to derive sediment and bubble particle subpopulations. Journal of Geophysical Research: Oceans 117, C007347

Twardowski, M.S., Boss, E., Macdonald, J.B., Pegau, W.S., Barnard, A.H., Zaneveld, J.R.V., 2001. A model for estimating bulk refractive index from the optical backscattering ratio and the implications for understanding particle composition in case I and case II waters. Journal of Geophysical Research 106, 14129–14142.

Tynes, H., Kattawar, G. W., Zege, E. P., Katsev, I. L., Prikhach, A. S., and Chaikovskaya, L. I., 2001. Monte Carlo and multi-component approximation methods for vector radiative transfer by use of effective Mueller matrix calculations, Appl. Opt., 40, 400-412.

Voss, K.J., Fry, E.S., 1984. Measurement of the mueller matrix for ocean water. Applied Optics 23, 4427– 4439.

Waquet, F., Cairns, B., Knobelspiesse, K., Chowdhary, J., Travis, L., Schmid, B., Mishchenko, M., 2009. Polarimetric remote sensing of aerosols over land. Journal of Geophysical Research-Atmospheres 114, D01206.

Waterman, T.H., 1954. Polarization patterns in submarine illumination. Science 120, 927-932.

Young, S.A., Vaughan, M.A., Kuehn, R.E., Winker, D.M., 2013. The retrieval of profiles of particulate extinction from cloud-aerosol lidar and infrared pathfinder satellite observations (CALIPSO) data: Uncertainty and error sensitivity analyses. Journal of Atmospheric and Oceanic Technology 30, 395-428.

Zaneveld, J. R. V., Kitchen, J. C. and Moore, C., 1994. The scattering error correction of reflecting-tube absorption meters," in Ocean Optics XII, S. G. Ackleson ed., Proc. SPIE 2258, 44-55.

E.P. Zege, I.L. Katsev, I.N. Polonsky, 1993. “Multicomponent approach to light propagation in clouds and mists”, Appl. Opt., **32**, 2803-2812.

E.P. Zege and L.I. Chaikovskaya, 1996. “New Approach to the Polarized Radiative Transfer Problem”, Journal of Quantitative Spectroscopy and Radiative Transfer, **55**, 19-31.

P.-W. Zhai, K. Knobelspiesse, A. Ibrahim, B.A. Franz, Y. Hu, M. Gao, and R. Frouin, "Water-leaving contribution to polarized radiation field over ocean," Opt. Express **25**, A689-A708 (2017)

Zibordi, G., Mélin, F., Berthon, J.F., Holben, B., Slutsker, I., Giles, D., D'Alimonte, D., Vandemark, D., Feng, H., Schuster, G., et al., 2009. AERONET-OC: a network for the validation of ocean color primary products. Journal of Atmospheric and Oceanic Technology 26, 1634-1651.

10. List of figure captions

Figure 1: The color coded segments illustrate the flight trajectory of the UC-12B involving overpasses at the location of the R/V Endeavor during the SABOR mission: station LS6 (open-ocean, 36.6512°N, 67.4267°W on 07/27/2014) and station LS9 (near-coastal, 36.9148° N, 75.8117° W on 07/30/2014). The inset in the lower left shows the remote sensing reflectance measured by the HyperSAS-POL instrument at the closest times to overpass. The shaded areas represent the standard deviation of 1-min averages close to the times of the UC-12B overpass at LS6 (blue) and LS9 (red).

Figure 2: Results from the typing algorithm based on the HSRL measurements of aerosol backscatter and extinction, for the UC12-B legs including the overpasses at stations LS6 (*upper panel*) and LS9 (*lower panel*). The yellow lines indicate the exact time of overpass. The presence in both scenes of variegate aerosol populations is evident.

Figure 3: The HyperSAS-POL instrument installed on the mast of the R/V Endeavor. An automated script fed by the ship navigational data commands a step-motor hidden below the baseplate to keep the instrument oriented towards sunglint-free angles.

Figure 4: Scattering phase matrix elements P11 and P21/P11 at 550 nm, for the aerosol models obtained for the LS6 and LS9 stations. For LS6, note the strong forward scattering peak (nearly two orders of magnitude higher than for LS9), and the complex behavior of the degree of linear polarization for both stations in the backscattering hemisphere.

Figure 5: *Left panels*: vertical profiles of particulate scattering and absorption as measured by the ac-9 measurements for stations LS6 (solid lines) and LS9 (thick dotted lines) at the wavelengths

indicated in color (the CDOM contribution is removed from the measured absorption). Note the marked increase in the scattering and absorption properties of the waters sampled at the near-coastal station LS9. *Right panel*: same as Fig. 4 (including the y-axes scales), but for the hydrosol models obtained for the LS6 and LS9 stations. The MVSM took measurements of P11 at a depth of 8 m. For LS9, one additional measurement was available at 3 m, which was used to describe the ocean layers above 6 m. For the DoLP, only 3 layers are shown for LS6 at depths as indicated by the numbers, in meters. For LS9, the polarization components resulting from the Mie simulations in 9 layers are indicated by fading shades of red, from the uppermost (2 m) to the deepest (10 m) layer.

Figure 6: *First Column*: Research Scanning Polarimeter measurements (solid) and model (dashed), color coded at the indicated wavelengths, for a near principal plane pass (the relative azimuth was 14°) over station LS6. The Solar Zenith angle was 38°. The scattering angles corresponding to the RSP viewing zenith angles (bottom x-axis) and relative azimuth are indicated in the top x-axis. The units for I, Q and U are [W m^{-2} μm^{-1} sr^{-1}]. *Second column*: same as in the first column, but for a flight transect oriented at 62°. The Solar Zenith angle was 36°. In order to retain the information on the sign of the polarization components when plotting in logarithmic scale, positive and negative branches of Q and U are explicitly indicated. *Third Column*: Same as previous columns, but for station LS9 and a flight transect oriented at 33°. The Solar Zenith angle was 31°. *Fourth column*: same as the third column but with an adjusted aerosol model as reported in Table 2. Red ovals indicate areas of sensible improvements in the quality of the fit.

Figure 7: Comparison between the hyperspectral Stokes vector measured by the HyperSAS-POL instrument (*left*: LS6; *right*: LS9) and the derived polarized radiance, $L_w^p = \sqrt{Q^2 + U^2}$ (gray), with RayXP model results (open circles). The simulations were performed with the same atmospheric

and oceanic inputs used to model the simultaneous RSP measurements (see Table 2 and Fig. 6), in order to demonstrated closure. The third row shows the total and polarized water-leaving radiances isolated from the measurements (note the log scale). The relative azimuth angles are 135° for LS6 and 225° for LS9. As in Fig. 6, the units of radiance are [W m^{-2} μm^{-1} sr^{-1}].

Figure 8: Reflectances associated with the Stokes parameters for the atmosphere-ocean system at the open-ocean station LS6, simulated at the top of the atmosphere for a downward-looking sensor at all viewing zenith (up to 80°) and azimuth angles.

Figure 9: As in Fig. 8, including the colorbars' limits, but for the near-coastal station LS9 and with the 670 nm band substituting the one at 470 nm.

Fig. 10: Spectral water-leaving radiances (in [W m^{-2} μm^{-1} sr^{-1}]) at the two stations for a viewing zenith angle of 40° as in Fig. 7, but in relation to the radiances calculated for the same angle at the TOA (*top row*). The bottom row contains the ratio of such radiances to quantify the contribution of Lw to radiances remotely sensed from orbit.

Figure 11: Absolute changes of TOA polarized reflectances at LS6 when a pure ocean is considered instead of the one characterized by the measured IOPs (Fig. 9), and under common atmospheric (no aerosols or with an oceanic type under 2km with spectrally flat AOT=0.1) and solar zenith angles (*left columns*: 20°; *right columns*: 50°). The angular ranges above and below the threshold for POLDER (see text) are highlighted.

Figure 12: As in Fig. 11, but for the near-coastal station LS9 and with the 670 nm band substituting the one at 470 nm.

Figure 13: Absolute differences in polarized reflectance between the LS6 and LS9 water types, simulated at the TOA under the same atmospheric conditions and viewing geometries as in Figs. 11 and 12. The green contour lines correspond again to the POLDER threshold (8.5×10^{-4}); purple ones to an achievable higher accuracy (1×10^{-4}). The values at 555 nm and 670 nm are below the POLDER threshold at all viewing geometries but become detectable at most viewing geometries with the new threshold.